Key Points:
- High-resolution Vs model of the whole Piton de la Fournaise Volcano
- The model highlights past and present main magma intrusion zones
- Radial anisotropy is a good indicator of the dominant fabric within a volcano

Correspondence to:
A. Mordret,
mordret@mit.edu

Three-dimensional shear velocity anisotropic model of Piton de la Fournaise Volcano (La Réunion Island) from ambient seismic noise

Aurélien Mordret[1,2], Diane Rivet[1,3], Matthieu Landès[1], and Nikolaï M. Shapiro[1]

[1]Laboratoire de Sismologie, Institut de Physique du Globe de Paris, Sorbonne Paris Cité, Paris VII-Denis Diderot University, CNRS (UMR 7154), Paris, France, [2]Now at Department of Earth, Atmospheric and Planetary Sciences, Earth Resources Laboratory, Massachusetts Institute of Technology, Cambridge, Massachusetts, USA, [3]Now at Université de Nice Sophia-Antipolis, CNRS, Observatoire de la Côte d'Azur, Géoazur UMR 7329, Valbonne, France

Abstract We cross correlate 4 years of seismic noise from the seismic network of Piton de la Fournaise Volcano (La Réunion Island) to measure the group velocity dispersion curves of Rayleigh and Love waves. We average measurements from vertical and radial components to obtain 577 Rayleigh wave dispersion curves. The transverse components provided 395 Love wave dispersion curves. We regionalize the group velocities measurements into 2-D velocity maps between 0.4 and 8 s. Finally, we locally inverted these maps for a pseudo 3-D anisotropic shear-velocity model down to 3 km below the sea level using a Neighborhood Algorithm. The 3-D isotropic shear-wave model shows three distinct high-velocity anomalies surrounded by a low-velocity ring. The anomaly located below the present "Plaine des Sables" could be related to an old intrusive body at the location of the former volcanic center before it migrated toward its present location. The second high-velocity body located below the summit of the volcano likely corresponds to the actual preferential dyke intrusion zone as highlighted by the seismicity. The third high-velocity anomaly located below the "Grandes Pentes" and the "Grand Brûlé" areas and is an imprint of the solidified magma chamber of the dismantled "Les Alizés" Volcano. Radial anisotropy shows two main anomalies: positive anisotropy above sea level highlighting the recent edifice of Piton de la Fournaise with an accumulation of horizontal lava flows and the second one below the sea level with a negative anisotropy corresponding to the ancient edifice of Piton de la Fournaise dominated by intrusions of vertical dykes.

1. Introduction

Seismic tomography is a powerful tool to image the seismic velocity structure of a volcano and therewith infer its geological history. Usual volcano tomographies rely on the inversion of *P* and/or *S* wave first arrivals from the local seismicity within or around the edifice [e.g., *Benz et al.*, 1996; *Lees*, 1992; *Lin et al.*, 2014; *Prôno et al.*, 2009; *Waite and Moran*, 2009; *Laigle et al.*, 2000; *Koulakov et al.*, 2011] or from active sources [e.g., *Aoki et al.*, 2009; *Tanaka et al.*, 2002; *Di Stefano and Chiarabba*, 2002; *García-Yeguas et al.*, 2012; *Shalev et al.*, 2010; *Zandomeneghi et al.*, 2013; *Hirn et al.*, 1999]. These methods are often hampered by the spatial and temporal distributions of the seismicity which partly controls the final resolution of the tomography or by the cost and difficulties to set up active seismic surveys in a rough environment. Ambient noise surface wave tomography, a method developed a decade ago, is one way to circumvent these issues.

1.1. Ambient Noise Surface Wave Tomography

It has been shown theoretically that the Green's function between different receiver locations can be retrieved from the cross correlation (CC) of sufficiently long recordings of a random wavefield for any inhomogeneous medium [e.g., *Weaver and Lobkis*, 2001; *Wapenaar*, 2004; *Gouédard et al.*, 2008]. In seismology, the seismic wavefield can be considered random for two kind of records: the coda of earthquakes [*Shapiro et al.*, 2000; *Campillo and Paul*, 2003] and long-time records of ambient seismic noise [*Shapiro and Campillo*, 2004]. Noise in the microseismic band is generated at the seafloor and mainly consists of fundamental mode surface wave energy [e.g., *Gutenberg*, 1958; *Bonnefoy-Claudet et al.*, 2006]. Therefore, the fundamental mode is most easily recovered in noise cross correlations between two stations. The main advantage of seismic noise is that it is available everywhere on Earth, at any time. Thus, using seismic noise CCs it becomes possible to perform surface wave tomography in areas without seismicity. Moreover, most of natural seismic noise energy comes from the secondary microseism band, between

1 and 10 s of period [*Longuet-Higgins*, 1950; *Hasselmann*, 1963; *Gualtieri et al.*, 2013]. These periods are too low to be generated with most of existing types of active sources. On the other hand, the surface waves at these periods are efficiently scattered by the heterogeneity of the crust over long distances and are thus quickly attenuated; they are not present in records from distant earthquakes or are too distorted to be easily used. At these periods, surface waves are mostly sensitive to the first tens of kilometers of the subsurface so ambient noise surface wave tomography has been widely used for continental- or regional-scale studies of the crust and the uppermost mantle [e.g., *Shapiro et al.*, 2005; *Sabra et al.*, 2005; *Moschetti et al.*, 2007; *Lin et al.*, 2007; *Yang et al.*, 2007; *Lin et al.*, 2008; *Zheng et al.*, 2008; *Stehly et al.*, 2009; *Zheng et al.*, 2011]. At smaller scale, ambient noise tomography has been used to image volcanic edifices at periods between 1 and 10 s: e.g., *Brenguier et al.* [2007] at Piton de la Fournaise Volcano, la Réuinon Island, *Masterlark et al.* [2010] at Okmok Volcano, Alaska, *Stankiewicz et al.* [2010] and *Jaxybulatov et al.* [2014] at Toba caldera, Indonesia, *Villagómez et al.* [2011] at Galápagos Archipelago, *Luzón et al.* [2011] at Deception Island, Antarctica, *Jay et al.* [2012] at Uturuncu Volcano, Bolivia, or *Nagaoka et al.* [2012] at Mount Asama, Japan.

In this study, we expand the work of *Brenguier et al.* [2007] by performing an ambient noise surface wave tomography of Piton de la Fournaise Volcano using a larger and denser seismic network. We invert jointly Rayleigh and Love wave group velocity dispersion curves to assess both the shear wave velocity and radial anisotropy structure of the volcano down to 3 km below sea level (bsl).

Joint inversion of Rayleigh and Love surface waves was widely used to study the radial anisotropy in the upper mantle on a global scale [e.g., *Anderson*, 1962; *Aki and Kaminuma*, 1963; *Montagner and Tanimoto*, 1991; *Ekström and Dziewonski*, 1998; *Shapiro and Ritzwoller*, 2002; *Beghein et al.*, 2006; *Becker et al.*, 2008]. In the past 10 years, radial anisotropy within the crust has been demonstrated in regions of active extension and crustal thinning, such as Tibet [e.g., *Shapiro et al.*, 2004; *Chen et al.*, 2009; *Duret et al.*, 2010], and western United States [*Moschetti et al.*, 2010; *Lin et al.*, 2011]. More recently, *Jaxybulatov et al.* [2014] used the surface wave derived radial anisotropy to characterize the horizontal layering of intrusions within a large volcano magmatic complex below the Toba caldera in northern Sumatra.

An anisotropic medium with hexagonal symmetry is characterized by five independent elastic coefficients A, C, N, L, and F [*Love*, 1927] linking the vertically and horizontally polarized compressional wave speeds (Vpv and Vph, respectively) with the vertically and horizontally polarized shear wave speeds (Vsv and Vsh, respectively) and density ρ. These coefficients are defined as $A = \rho Vph^2$, $C = \rho Vpv^2$, $N = \rho Vsh^2$, $L = \rho Vsv^2$, and F is related to the speed of waves traveling at intermediate incident angles and is often defined as $F = \eta(A - 2L)$, with $\eta \neq 1$ for anisotropic medium. In such medium surface waves traveling horizontally with a vertical polarization (Rayleigh waves) travel at Vsv speed whereas horizontally polarized waves (Love waves) travel at Vsh speed. Rayleigh waves, with their elliptic polarization, present a small sensitivity to Vsh which will be neglected in this study. The difference between these wave speeds is called radial anisotropy, which is represented here as the percentage difference between Vsh and Vsv in the medium

$$\xi = \frac{Vsh - Vsv}{Vs}. \tag{1}$$

In this case, if the P wave radial anisotropy and the effect of η are neglected, Vs is the isotropic or effective S wave velocity and is computed from Vsh and Vsv via a Voigt's average which better reflects the isotropic variations in elastic properties [*Dziewonski and Anderson*, 1981; *Ekström and Dziewonski*, 1998]:

$$Vs = \sqrt{\frac{2Vsv^2 + Vsh^2}{3}}. \tag{2}$$

This paper presents the first study measuring radial anisotropy at the scale of a volcano. In a volcanic context, but at a regional scale (~ 100 km $\times$ 100 km), *Jaxybulatov et al.* [2014] measured radial anisotropy at Lake Toba (Indonesia) to find a large magmatic sill complex beneath the caldera.

The tomography is performed using a common three-strep approach [e.g., *Ritzwoller et al.*, 2011]. First, frequency-dependent group travel times are measured from every interstation noise CC (section 2). In the second step, the surface wave travel times are inverted to construct 2-D group velocity maps at different frequencies (section 3). The final step is to invert the dispersion maps for the depth structure. This last step consists of inverting regionalized dispersion curves for a local 1-D shear velocity model in every cell of the geographical grid. Combining all 1-D profiles from all cells, result in the final 3-D model of the volcano (section 4).
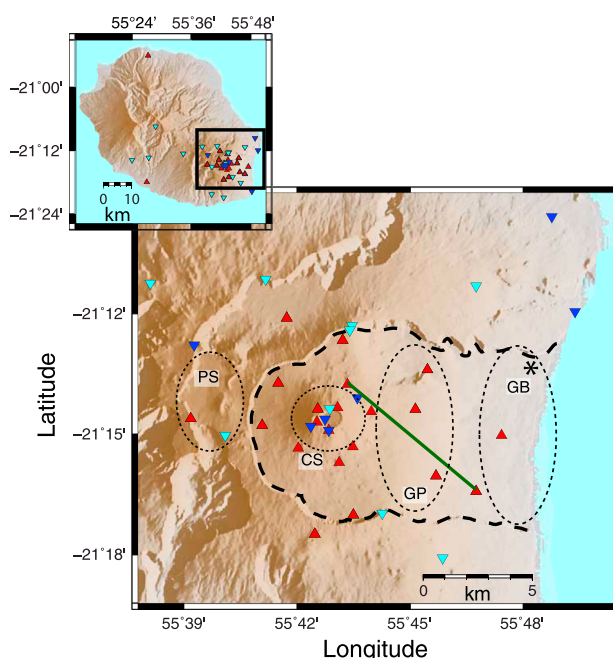
Figure 1. Map of Piton de la Fournaise Volcano area and parts of the seismic network used in this study. Broadband seismometers are displayed with red triangles and short-period seismometers are displayed with reverse triangles. Three-component short-period sensors are shown by blue and one-component short-period sensors by cyan triangles. The green line highlights the path between station FJS and UV02 used in Figure 3. The names of the different parts of the volcano are also written and highlighted by the ellipses: PS - Plaine des Sables, CS - central summit, GP - Grandes Pentes, and GB - Grand Brûlé. The contour of the Enclos Fouqué caldera is shown by the black dashed line. The asterisk shows the location of the Grand Brûlé drilling. Inset: map of the Reunion Island with the complete network used in this study. The rectangle shows the studied area. The topography is shown by the brown-shaded background.

1.2. Geological Setting

Piton de la Fournaise (PdF, Figure 1) is a basaltic-shield volcano located on the eastern side of La Réunion Island in the western Indian Ocean. It is the most recent manifestation of La Réunion hot spot which was also responsible for the creation of the Deccan traps [*Courtillot et al.*, 1986]. PdF is one of the most active volcanoes in the world with an average of three eruptions per year between 2000 and 2010. Geological and geophysical studies have shown that the recent edifice was built, starting about 530 ka ago, on two ancient inactive volcanoes: Piton des Neiges and Les Alizés Volcanoes. Between 150 ka and 12 ka, both Piton des Neiges and PdF were active, and after 12 ka, the eruptive activity has been restricted to PdF [*Lénat et al.*, 2001; *Michon et al.*, 2007; *Merle et al.*, 2010; *Lénat et al.*, 2012]. History of PdF has been marked by major geological events like caldera collapses intersected by gigantic landslides [e.g., *Merle et al.*, 2010]. The last landslide, 150 ka ago, was accompanied by an eastward shift of the volcanic center from the present-day location of the Plaine des Sables (Figure 1) to the present PdF central cone [*Letourneur et al.*, 2008; *Merle et al.*, 2010]. This ancient volcanic center has built a large and dense hypovolcanic complex which has been revealed by gravimetric measurements

[*Rousset et al.*, 1989; *Malengreau et al.*, 1999; *Gailler et al.*, 2009]. The latest evolution stage of PdF is marked by the Enclos Fouqué caldera formation about 4.5 ka ago [*Staudacher and Allègre*, 1993]. Since then, most of the eruptions took place inside the Enclos caldera or along preferential fractured intrusion zones called rift zones.

Les Alizés Volcano, presently completely eroded, had its volcanic center slightly East of PdF present summit, below the Grand Brûlé plain. The evidences of its existence are (1) a large intrusive complex found 1000 m below the surface by drilling in the Grand Brûlé [*Rançon et al.*, 1989, Figure 1], (2) a large gravimetric anomaly indicating a dense intrusive core [*Rousset et al.*, 1989; *Malengreau et al.*, 1999; *Lénat et al.*, 2001; *Gailler et al.*, 2009; *Gailler and Lénat*, 2012], and (3) reverse magnetic anomalies which characterize rocks older than those of PdF [*Lénat et al.*, 2001; *Gailler and Lénat*, 2012].

2. Noise Correlations and Dispersion Curve Measurements

2.1. Data and Preprocessing

We use continuous seismic noise records of both short-period and broadband seismic sensors which were operating during and following the UnderVolc temporary project. During this experiment, which started in September 2009 and ended in June 2011, a high-resolution seismic network with 15 broadband seismic stations was deployed on PdF Volcano [*Brenguier et al.*, 2012]. In addition to UnderVolc stations, we used data recorded by six permanent broadband stations installed and maintained by the PdF Volcano observatory. After the end of the UnderVolc experiment, most of these sites were reequipped with
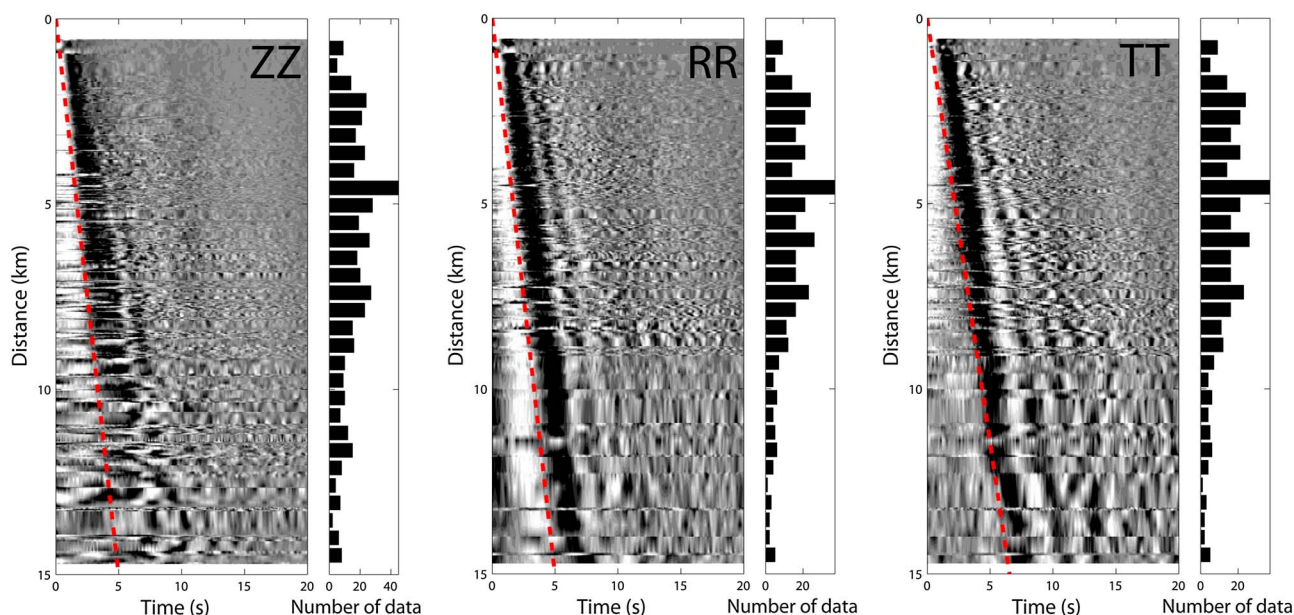
Figure 2. Correlations used in this study (limited to 15 km interstation distance) for the ZZ, RR, and TT components, filtered between 0.05 and 5 Hz. Insets at the right of the correlations shows the number of correlations in different interstation distance bins. The red dashed lines in the ZZ and RR panels show the 3 km/s moveout. The red dashed line in the TT panel shows the 2.4 km/s moveout. Notice that the spatial coherency of the horizontal components (RR and TT) is higher than the one of the vertical component.

permanent broadband seismometers. Overall, we use continuous records of 21 broadband stations during UnderVolc experiment and records from January 2011 to September 2013 of 19 broadband sensors and of 21 short-period sensors of PdF Volcano observatory following UnderVolc experiment. Among the short-period sensors used in this study, 13 are single vertical-component stations (Figure 1).

The procedure for seismic data processing and computing seismic noise CCs is described hereafter. After band-pass filtering continuous signals between 0.05 and 5 Hz, a frequency band where the amplitude of the ambient noise on the Réunion Island is expected to be high, we eliminate portions of signals with amplitude greater than 10 times the standard deviation calculated for the entire day. We then apply a complete spectral whitening between 0.05 and 5 Hz on the ambient noise records. Then, signals with amplitude greater than 3 times the standard deviation are discarded. This preprocessing helps to remove the effect of small local seismic events. Finally, we applied a 1 bit normalization on the whitened noise records. We compute daily CCs of one-bitted and whitened continuous noise between pairs of stations that span the same time period.

For three-component sensors in addition to vertical-vertical (ZZ) component CCs, we compute also the north-north (NN), north-east (NE), east-east (EE), and east-north (EN) CCs. The transverse-transverse (TT), transverse-radial (TR), radial-radial (RR), and radial-transverse (RT) CCs between each station pair are calculated by a tensor rotation [*Lin et al.*, 2008]. Finally, we stack all available daily CCs for each pair of stations to enhance the SNR, and we retain their symmetric parts by averaging their positive and negative lag times. We end up with a total of 577 ZZ-component CCs and 395 TT and RR-component CCs. Figure 2 shows all CCs used in this study. The panels on the right of the CCs present an histogram of the number of CCs in different interstation distance bins. The largest number of CCs is found for interstation distances < 10 km. They correspond to station pairs inside the Enclos Fouqué caldera. It can also be noted that the horizontal components (RR and TT) exhibit a different frequency content compared to the ZZ components. They also have a better spatial coherency. Finally, the moveout of the TT components is slower (∼2.4 km/s) than the moveout of the ZZ and RR components (∼3 km/s).

2.2. Dispersion Measurements Using FTAN

We measure group velocities of surface waves extracted from noise CCs between pairs of stations using the frequency-time analysis (FTAN) [*Levshin et al.*, 1989]. Group velocities dispersion curves are initially estimated automatically. However, for some CCs the automatic picking of the dispersion curves in the time-frequency
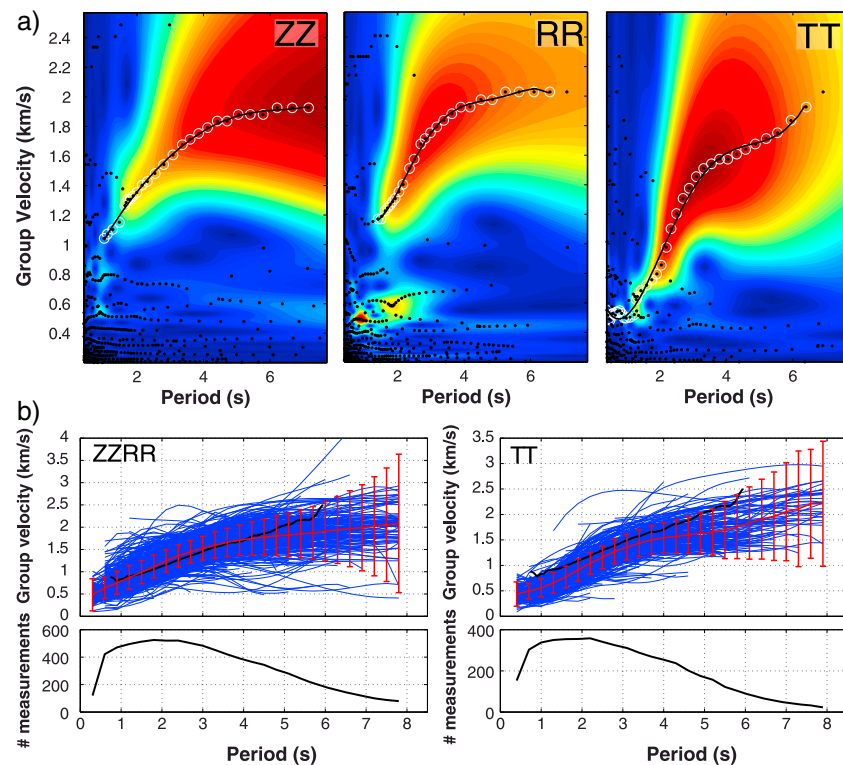
Figure 3. Group velocity dispersion curve measurement via frequency-time analysis (FTA). (a) Example of dispersion curve automatic picking on FTA diagrams for ZZ-, RR-, and TT-component correlations. The colored background shows the FTA diagram with reddish colors showing the large amplitudes. Black dots show the relative maxima of the diagram, the white circles around some maxima highlight the automatically picked dispersion curve. The black line is a five-order polynomial fitting the dispersion curve. (b) Every Rayleigh (left) and Love (right) dispersion curves used in this study. Red curves with error bars show the average dispersion curves with their standard deviations. The thick black line (the same in left and right panel) is the average Rayleigh wave group velocity dispersion curve measured by *Brenguier et al.* [2007]. Note the good agreement at short period for ZZRR component. Bottom panels show the number of measurements as a function of the period.

diagrams is not correct. CCs may contain high-amplitude surface wave overtones or scattered waves that lead to a wrong automatic picking of the dispersion curve. Because this problem appears for many CC, we developed a Graphical Users Interface (available upon request from the corresponding author) that involves analyst validation. In this way, we were able to mitigate the false detections due to overtones or multipathing. Figure 3a shows period-velocity diagrams for the station pair FJS-UV02 (Figure 1) for the three ZZ, RR, and TT components. ZZ- and RR-component CCs are used to estimate Rayleigh waves dispersion curves and TT component are used to estimate Love wave dispersion curves. The black dots are showing the different local maxima of the diagrams, and white circles show the manually validated maxima corresponding to the fundamental mode. The measurements are done at periods corresponding to interstation distances larger than 1.5 wavelength. Finally, the dispersion curves are interpolated and smoothed by a fifth-order polynomial (Figure 3a, black curve), and the ZZ and RR dispersion curves for identical paths are averaged to reduce the noise measurement. In the example of Figure 3a, the ZZ and RR dispersion curves are similar, but they are picked in a different period band and they exhibit small discrepancies which can be reduced by averaging, making the measurement more robust and covering a larger period band.

Figure 3b shows the final set of Rayleigh (ZZ, RR) and Love (TT) dispersion curves. The red curves with error bars are the mean dispersion curves with their standard deviation at each period. These error bars will be used as velocity uncertainties of the local dispersion curves during the depth inversion procedure (see section 4 for details). The black curve in the top frames of Figure 3b is the average dispersion curve obtained by *Brenguier et al.* [2007]. Our measurements are in very good agreement with their data between 2 and
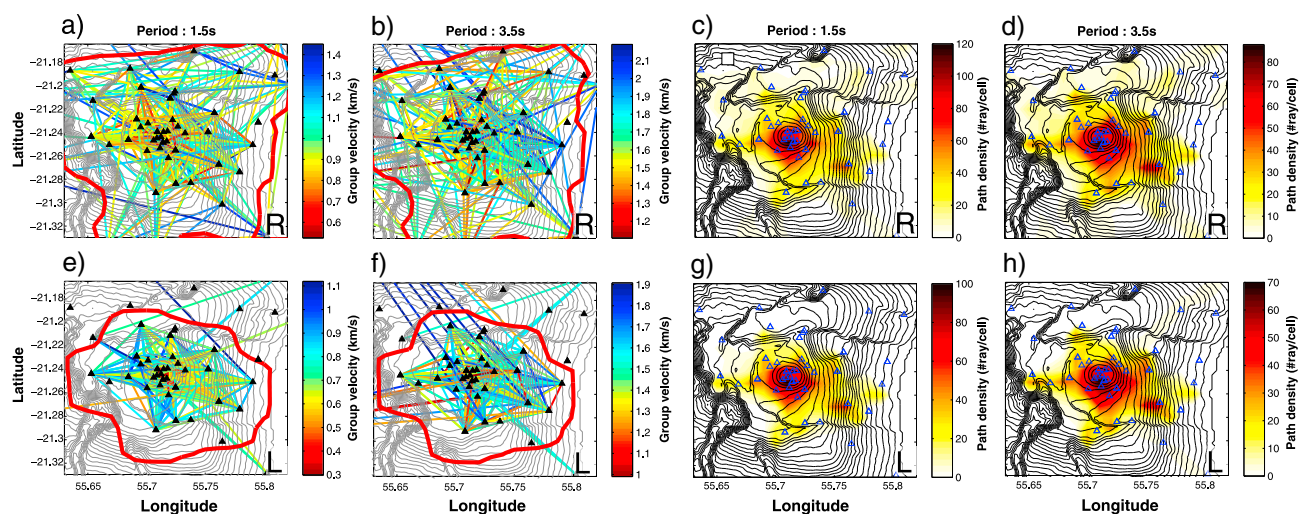
Figure 4. Group velocity measurements and coverage at 1.5 s and 3.5 s for Rayleigh (top) and Love waves (bottom). (a, b, e, f) Colored lines reflect the group velocity associated with each path at 1.5 and 3.5 s. The red contour shows the smoothed level of four paths per cell. Black triangles are the seismic stations. Topography is shown by gray contours. (c, d, g, h) The path density at 1.5 and 3.5 s for Rayleigh and Love waves. Stations are blue triangles, and topography is shown by black contours. The black square in Figure 4c represents the size of one cell of 1 km by 1 km.

4.5 s, the period band they found reliable. The discrepancy in the longer periods may be due to the fact that they solely used short-period sensors in their study and have very few measurements above 5 s, preventing them from retrieving accurate long-period signals. Because most of our long-period measurements come from the broadband sensors, we think that if a bias from the short-period sensors exists, it does not impair the results of our tomography at long period. Besides, it appears that the Love wave dispersion curves are in average slower than the Rayleigh wave ones, confirming the observation on the individual CCs (Figure 2).

3. Rayleigh and Love Wave Group Velocity Maps

Figures 4a, 4b, 4e, and 4f show the measured group velocities at 1.5 and 3.5 s for Rayleigh and Love waves, respectively, where lateral velocity variations can be observed. The ray coverage shown in Figures 4c, 4d, 4g, and 4h is dense, especially around PdF summit. We used a grid composed of 28 × 31 square cells with a grid size of 1 km. The whole Enclos Fouqué caldera and Plaine des Sables exhibit a reasonable coverage at all periods with more than 10 rays per cell. The red contour in Figures 4a, 4b, 4e, and 4f delimits a smoothed four-rays-per-cell level where fair results are expected to be retrieved. We inverted these measured group velocities with the method of *Barmin et al.* [2001] which is based on ray theory involving a regularization function. This function is composed of a spatial Gaussian smoothing function and a constraint on the amplitude of the perturbation depending on local path density. The Cartesian version of this method used for the present study has been described in details by *Mordret et al.* [2013]. We inverted the measured Rayleigh and Love wave dispersion curves group velocity maps at 78 periods between 0.3 and 8 s and 52 periods between 0.4 and 5.5 s with 0.1 s steps for Rayleigh and Love waves, respectively. The initial model had a constant velocity equal to the mean group velocity for each period. We performed the inversion in two steps [*Moschetti et al.*, 2007]. First, we inverted a very smooth map that was used to identify and reject outliers (measurements with travel time residuals greater than two standard deviations). The remaining measurements were used in the second step of tomography to produce the final group velocity map. We do not take into account the topography during the inversion procedure. We estimate the errors introduced by this approximation as the relative difference in distance between the stations with or without taking into account their difference in elevation. The errors are thus simply the relative difference between the base of a right triangle and it hypotenuse. We found error <5% (Figure 5) on group velocity measurements, with more than 90% of the paths having errors <3%. The group velocity measurements show variations of more than 30% at a each period (Figure 4). The errors caused by the flat topography approximation should be, therefore, negligible.
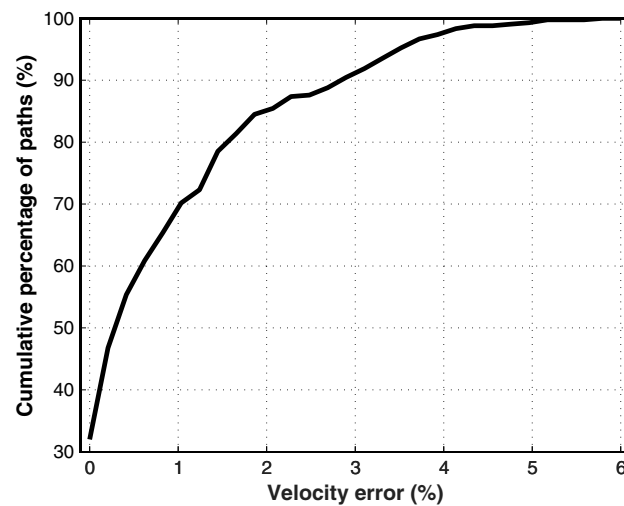
Figure 5. Velocity error introduced by neglecting the topography. The curve shows the cumulative number of paths having errors smaller than a certain threshold. 90% of the paths has error smaller than 3%.

3.1. Group Velocity Maps

Figures 6 and 7 show the group velocity maps at four different periods (0.6, 1.5, 3.5, and 5 s) for Rayleigh and Love waves, respectively. Only the locations with more than four rays per cell are shown and interpreted. The variance reduction of the travel time residual generally exhibits values higher than 50% indicating that the retrieved velocity maps fit the data reasonably well. The mean velocity of the maps increases with the period for both Rayleigh and Love waves, in good agreement with the mean dispersion curves shown in Figure 3. At short period, the summit of PdF is marked by lower velocities surrounded by a high-velocity ring (Figures 6a, 6b, 7a, and 7b), whereas at longer periods a high-velocity anomaly is observed below the summit with lower velocity around (Figures 6c, 6d, 7c, and 7d).

3.2. Resolution Assessment

To estimate the accuracy of the size and location of the retrieved anomalies, the spatial resolution of each map has been assessed through the evaluation of the resolution matrix associated with each inversion
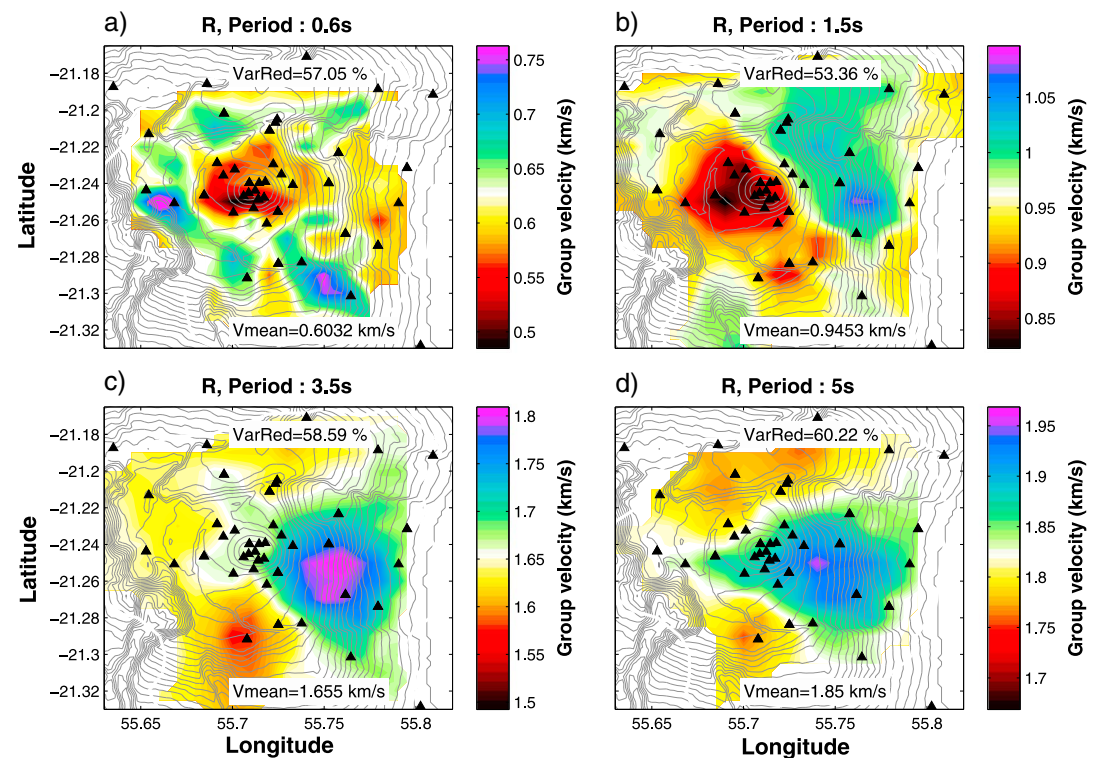

Figure 6. Rayleigh wave group velocity maps at 0.6, 1.5, 3.5, and 5 s. The seismic network is shown by the black triangles and the topography by the gray contours. For each map, the variance reduction between data computed from a homogeneous model with an average velocity and the final model is shown at the top of the frames. The final mean velocity is shown at the bottom of each frame. Note the inversion of velocity structure between short periods and long periods with a low-velocity anomaly around the summit surrounded by a high-velocity ring at short periods and high velocities below the summit with low velocities around at long periods.
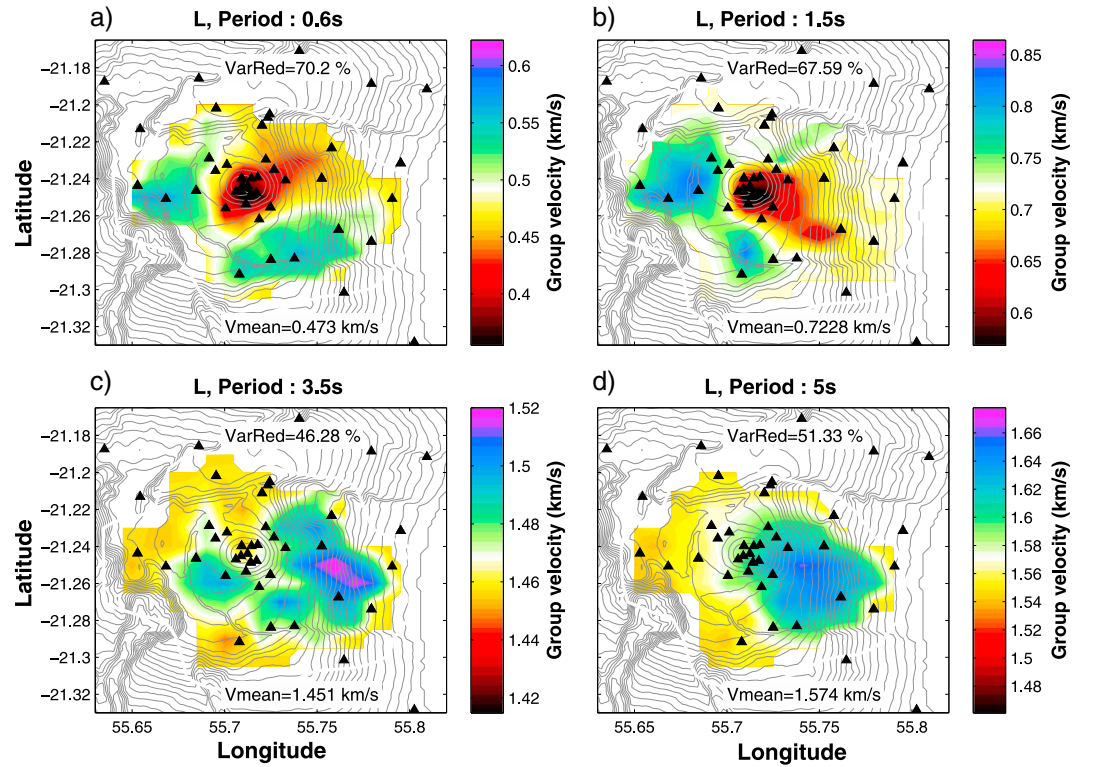
Figure 7. Same as Figure 6 but for Love wave group velocity maps. Note the same global velocity structure pattern as for Rayleigh waves.

[*Barmin et al.*, 2001; *Mordret et al.*, 2013]. Each line of the resolution matrix represents the response of the tomographic process to a Delta function type anomaly located in a corresponding cell of the model. The size, the shape, and the location of the output spot given by the resolution matrix indicate how accurately the tomography is able to retrieve the anomaly. Figures 8a and 8c show two examples of the input spike at two different locations on the volcano, for Rayleigh and Love waves at 0.6 s, respectively. Figures 8b and 8d show the corresponding lines of the resolution matrix represented as contour maps. One can see how the input spike has been modified by the tomography process, both in shape, amplitude, and location. To extract more quantitative information from these maps, we roughly follow the idea of *Fichtner and Trampert* [2011] and fitted an ellipse (in black in Figures 8b and 8d) to the contour level at 40 % of the maximum (Figures 8b and 8d, blue). The coordinates of the center of the ellipse, (x_e, y_e), its area, S_e, as well as the length, b_e and azimuth, θ_e of its major axis, are extracted to represent the resolution of our tomography. We first represent the resolution shift (R_{shift}, Figures 9a, 9c, 9e, and 9g) which is the distance between the targeted cell of coordinates (X_0, Y_0) and the center of the ellipse and expressed as

$$R_{shift} = \sqrt{(X_0 - x_e)^2 + (Y_0 - y_e)^2} .$$ (3)

In the case of our study, the size of the cells is 1×1 km; thus, a resolution shift smaller than 0.5 km indicates that the anomaly is located at the right place, within the targeted cell. One can see that anomalies located around PdF summit and in most of parts of the Enclos Fouqué are well located.

We then represent the spatial resolution, R, (Figures 9a, 9c, 9e, and 9g) which is the effective diameter of the spot of the resolution matrix and indicates the maximum reliable size of the retrieved anomalies by

$$R = 2\sqrt{\frac{S_e}{\pi}} .$$ (4)

These values are shown by the color background of Figures 9b, 9d, 9f, and 9h. The spatial resolution is limited at a minimum of 2 km, the minimum size to be able to separate two neighbor anomalies.
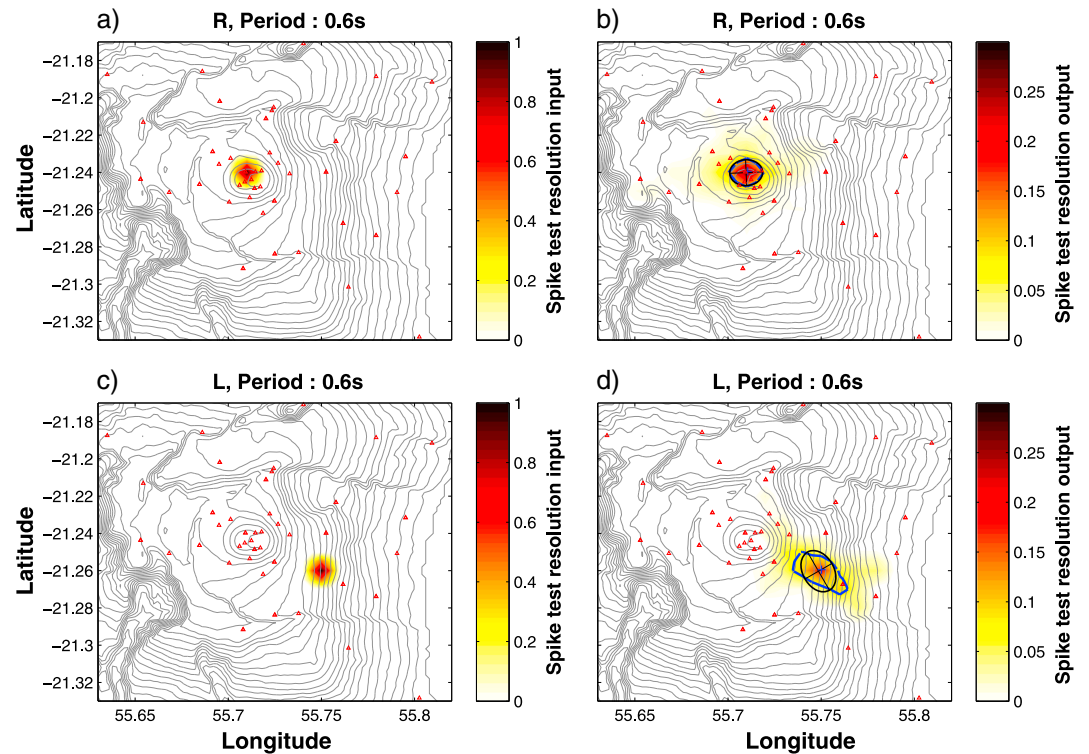
Figure 8. Method for the spatial resolution assessment. (a, c) Input spike at 0.6 s at two different locations for Rayleigh and Love wave, respectively. (b, d) Row of the resolution matrix associated with the location of the input spikes and displayed as a map. The blue cross is the location of the input spike, the blue contour is the contour level at 40% of the maximum amplitude of the output spot. To assess the spatial resolution, an ellipse, in black, is fitted to this contour. The minor and major axes of the ellipse (black lines), their azimuths, as well as the coordinates of its center are extracted.

The strength and direction of smearing of the anomalies are given by b_e and θ_e represented as black lines in Figures 9b and 9h.

In general, where the ray coverage is dense (in the Enclos), the spatial resolution is smaller than 3–4 km, and the smearing is weak. The central cone is very well resolved at all periods. Away from the volcano, the resolution is strongly controlled by the geometry of the network with radial smearing pointing toward the summit. We will discuss the final 3-D model in the light of these spatial resolution results in section 6.

4. Inversion of Local Dispersion Curves With the Neighborhood Algorithm

Group velocity maps for Rayleigh and Love waves can be seen as the gather of local group velocity dispersion curves: for one particular location one has group velocity measurements at different periods. These local dispersion curves can be inverted to assess a 1-D local layered velocity model. To do so, we used the Neighborhood Algorithm (NA) developed by *Sambridge* [1999]. The NA is a Monte Carlo global direct-search technique developed to efficiently sample a model space (see *Sambridge* [1999] and *Mordret et al.* [2014] for a complete description of the algorithm and method used in this paper).

4.1. Parameterization

Because Rayleigh waves and Love waves are primarily sensitive to Vsv and Vsh, respectively, and in order to reduce the number of free parameters, we make the (nonphysical) simplification of restricting the anisotropy to S wave velocity, allowing Vsh to differ from Vsv but setting Vpv = Vph and $\eta = 1$. Under these circumstances, *Xie et al.* [2013] showed that the inferred anisotropy, regardless of its sign, may be slightly underestimated. However, the difference between the results obtained using only Vsv and Vsh and the results obtained using the five coefficients is small and lays within the uncertainties.

In the local dispersion curve inversion problem, for the isotropic case, the model is usually a 1-D layered S wave velocity profile where the parameters are the thickness and the velocity in each layer. The drawback
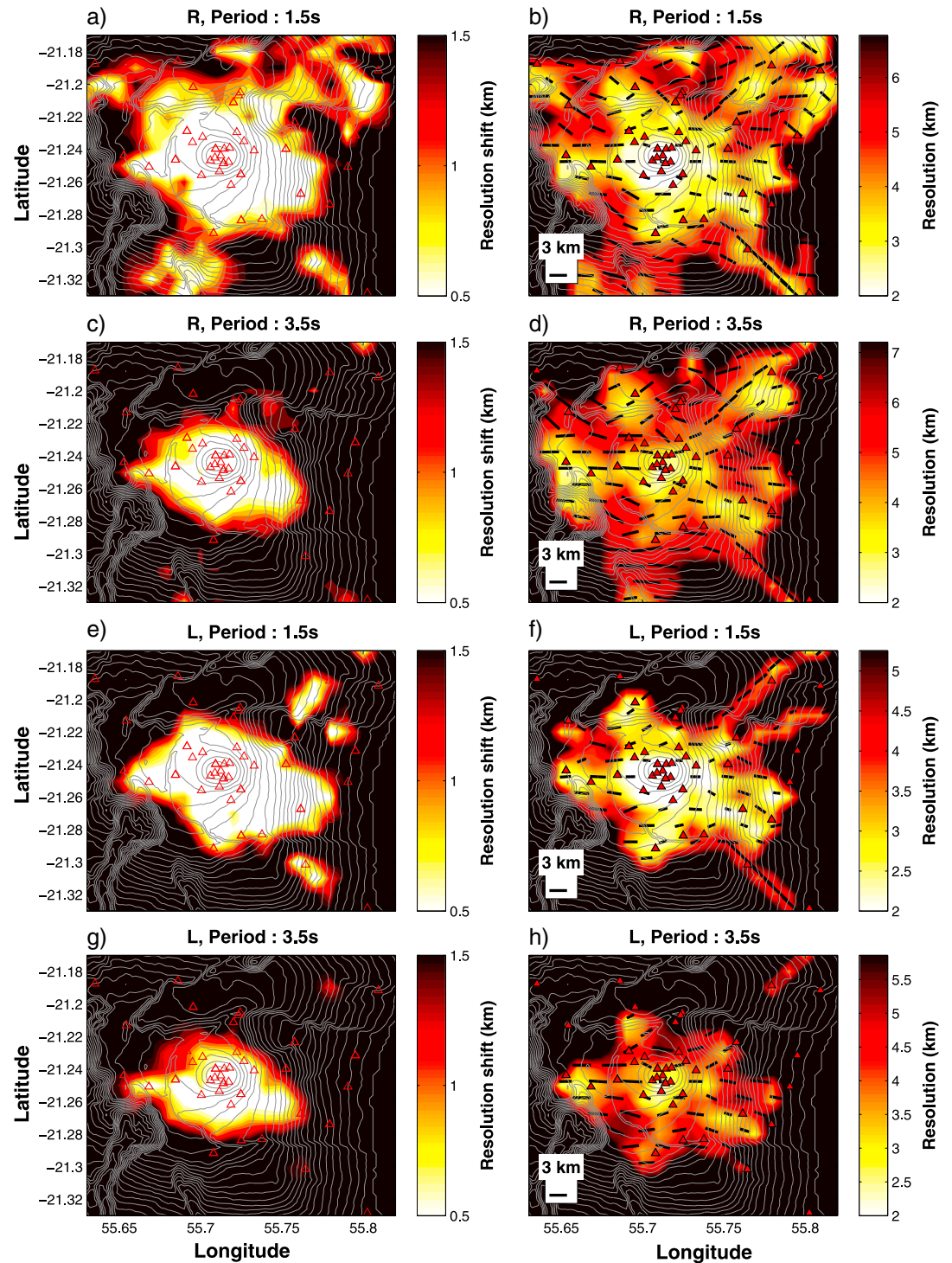
Figure 9. Spatial resolution results for Rayleigh waves at (a, b) 1.5 s and (c, d) 3.5 s and for Love waves at (e, f) 1.5 s and (g. h) 3.5 s. Figures 9a, 9c, 9e, and 9g show the resolution shift R_{shift} (equation (3)). A resolution shift <0.5 km means that the center of the retrieved anomaly is in the same cell as the input spike. Figures 9b, 9d, 9f, and 9h show the spatial resolution maps. The black lines give the strength and direction of the smearing as the length and azimuths of the major axis of the ellipses (see text for details). The scale is given in the bottom left corner. In all frames, triangles are seismic stations, and topography is shown by the gray contours.
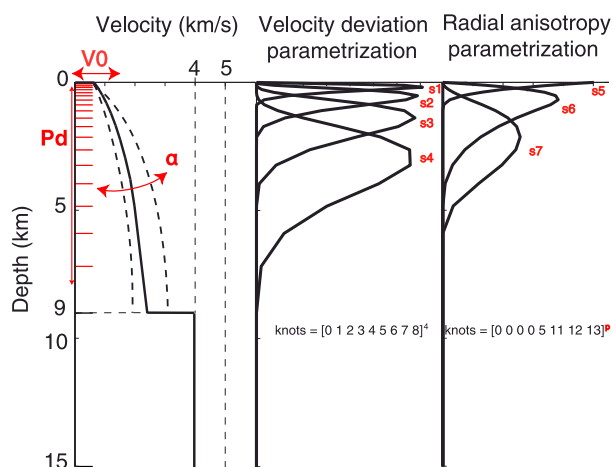
Figure 10. Model parameterization including 11 parameters: (1) P_d controls the layer depths, (2) V_0, surface velocity, (3) α, the curvature of the velocity profile, (4–7) cubic B spline perturbations to the power law S wave velocity profiles, S_1 to S_4, (8–10) cubic B spline radial anisotropies, S_5 to S_7, and (11) a power p for the anisotropy spline knots controlling the depth extent of the anisotropy.

of this parameterization is that one has to invert for $2n_l$ parameters, where n_l is the number of layers. If n_l is chosen too large, the volume of the model space becomes immense, and it is very time-consuming to sample it densely enough. This parameterization becomes unrealistic if one adds a third parameter for an anisotropic inversion. Besides, too many parameters also result in an over parameterization of the inverse problem which leads to badly constrained solutions. To reduce the number of parameters, we follow *Mordret et al.* [2014] and parameterize the 1-D S wave velocity model with 11 parameters: 10 of them describe the velocity values at each depth and the last one is used to constrain the layer depth distribution. We use a power law backbone velocity profile to take into account the possible slow velocities in the shallow layers due to weathering and alteration. This backbone is overlaid with smoothly varying velocity anomalies and anisotropy. Figure 10 summarizes the parameterization with the 11 parameters highlighted in red. See the appendix for a detailed description of the parameterization. The allowed range for each parameter is shown in Table 1.

Because of the weaker sensitivity of surface waves to P wave velocities and densities, these quantities are not considered as free parameters and are set using relationships from a former study at PdF Volcano: Vp (km/s) $= 0.3D+3$ [*Prôno et al.*, 2009] with D the depth in kilometers and ρ (g/cm^3) $= (Vp+2.37)/2.81$ with Vp in km/s [*Gebrande*, 1982]. Tests showed that the choice of the relations linking Vp to ρ had negligible effects on the inversion results. Besides, the attenuation is not taken into account by setting the quality factor Q infinite. This parameterization is constant across the whole studied area.

4.2. Inversion Procedure

With the parameterization and simplifications described above, we invert local dispersion curves at depth using the NA for the model space exploration and the subroutines from the Computer Programs in Seismology package [*Herrmann and Ammon*, 2004] for the forward modeling. We used the same forward modeling method as *Mordret et al.* [2014], with a modification to take into account the radial anisotropy. This is done in the following way: a model is randomly chosen by the NA and is attributed to Vsv, a synthetic Rayleigh wave dispersion curve is computed and the misfit Mr between the measured and synthetic Rayleigh-wave dispersion curves is stored. Then, the same model, with the same parameters is perturbed by including the anisotropy and is attributed to Vsh. A synthetic Love wave dispersion curve is computed and the misfit Ml between the measured and synthetic Love wave dispersion curves is stored. The final combined misfit M is computed as $M = 0.4Ml + 0.6Mr$ to take into account the fact that Love wave dispersion curves have a smaller

Table 1. Ranges Allowed for the Inverted Parameters

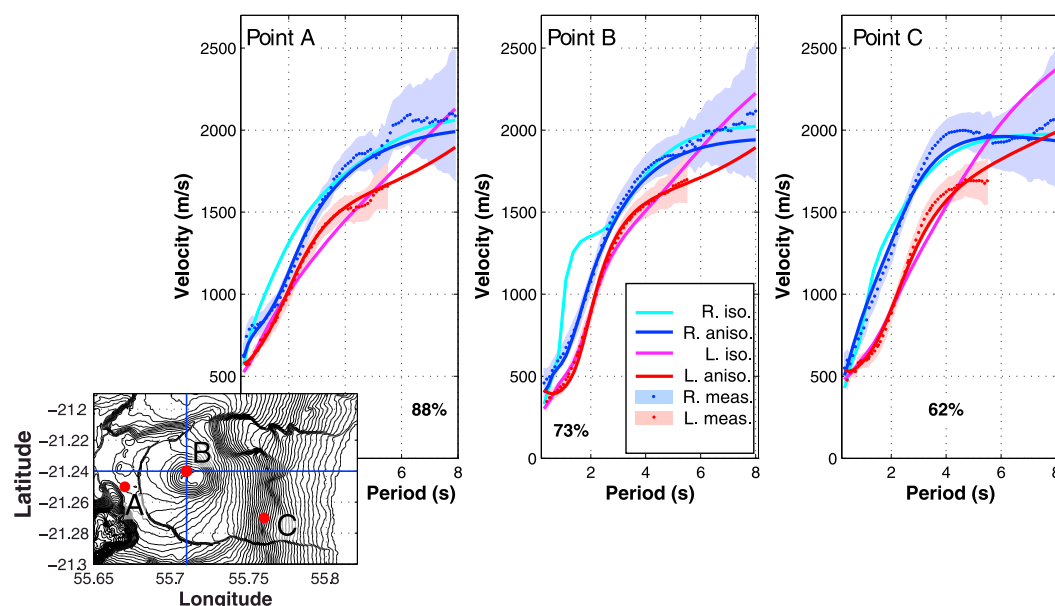| Parameters	Allowed Range
V_0	550–750 m/s
α	0.2–0.24
P_d	400–700 m
S_1	± 30%
S_2	± 30%
S_3	± 30%
S_4	± 30%
S_5	−50–20%
S_6	−20–50%
S_7	−50–20%
p	2–4

Figure 11. Best synthetic Rayleigh and Love group velocity dispersion curves at points A, B, and C (see the inset for locations) for an isotropic and anisotropic inversion. The cyan and magenta curves are the best fitting isotropic dispersion curves for Rayleigh and Love waves, respectively. The blue and red curves are the best fitting anisotropic dispersion curves for Rayleigh and Love waves, respectively. The blue and red dots with the blue and red areas are the measured Rayleigh and Love wave dispersion curves, respectively, with their uncertainties. The percentages at the bottom of the frames are the misfit reduction between isotropic inversion and anisotropic inversion indicating the necessity of anisotropic parameterization. Blue lines in the inset show the location of the profiles displayed in Figures 15 and 18.

number of point fitted (shorter period band) with four more parameters. For both Rayleigh and Love dispersion curves, the misfit is defined as an area ratio between the synthetic dispersion curves and the measured dispersion curve with its uncertainties (see *Mordret et al.* [2014] and their Figure 2 for a more detailed description). The standard deviation used as uncertainty accounts also for the velocity lateral variations. However, we found that the standard deviation qualitatively mimics the uncertainties that one would expect from the FTAN measurements, i.e., a relative broadening of the uncertainties with increasing periods. Moreover, the values of the uncertainty used in the depth inversion are only relative from one frequency to another: multiplying all uncertainties by a common factor will change the final value of the misfit but it will not change the position of its minimum value. Therefore, we believe that the choice of the standard deviation as uncertainty does not affect much our inversion.

In total, 31,000 Vsv and Vsh models are sampled for each location. The best 1000 models are kept to create on the one hand a set of 1000 Voigt's average isotropic shear wave velocity models (Vs), and on the other hand, a set of 1000 radial anisotropy models (ξ) using equations (2) and (1). Then, results are summarized by computing the nonweighted mean and standard deviation of the mean of these two sets.

To assess the necessity of introducing radial anisotropy, we also performed an inversion without the four parameters describing the anisotropy, setting Vsv = Vsh = Vs. Figure 11 shows the best fit to isotropic and anisotropic dispersion curves at three different locations. On average over the whole studied area, anisotropic parameterization reduces the misfit by ~ 70%.

5. Results

5.1. Example of Local 1-D Model

As example of local dispersion curve inversion using the NA, let us consider the point B shown in Figure 11. It is located near PdF summit. Figure 12 presents the Vsv and Vsh models obtained by inversion as well as the synthetic dispersion curves associated with each sampled model. The color defines the misfit. Black crosses with the error bars in the top row are the measured local dispersion curves. The middle row shows the inverted Vsv and Vsh models with the thick black line being the average of the 1000 best models which
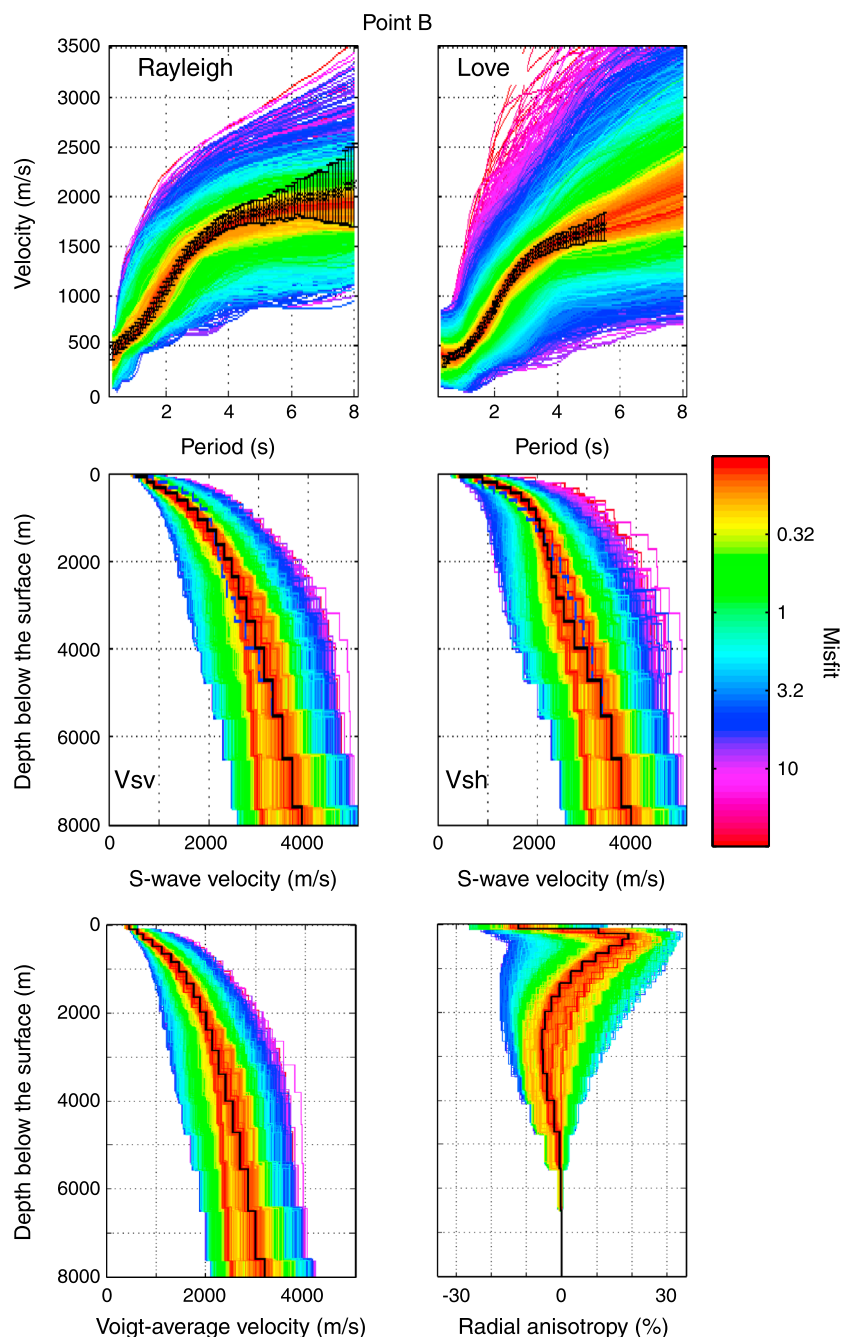
Figure 12. Inverted models and local dispersion curves for point B (Figure 11). (top row) The local dispersion curves for Raleigh (left) and Love (right) waves as black crosses with error bars overlaying the synthetic dispersion curves associated with the 31,000 models sampled by the Neighborhood Algorithm. The synthetic models are colored according to their misfit. (middle row) The 31,000 sampled Vsv (left) and Vsh (right) models colored according to their misfit. The thick black model is the average of the 1000 best models, the dashed blue model is the average of the 1000 best models for the other anisotropic velocity plotted for comparison. (bottom row) The Voigt-averaged isotropic Vs models (left) and the corresponding radial anisotropy models (right).

will be used to build the final 3-D velocity model. Thick dashed blue lines are the average of the 1000 best models for the other velocity for comparison. For every location of the model, the misfit of the best 1000 models is < 0.3. The bottom panel shows the Voigt-averaged isotropic Vs model and the radial anisotropy. Above 2 km depth (with respect to the local altitude), Vsh is constantly higher than Vsv suggesting a strong positive radial anisotropy. Below 2 km depth, the contrary is observed with Vsh smaller than Vsv, suggesting
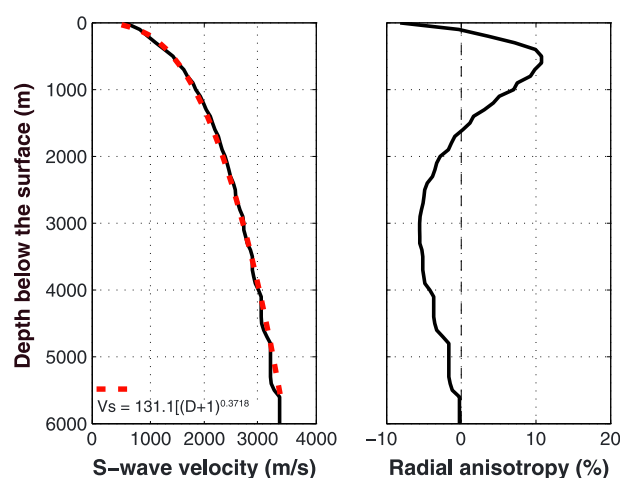
Figure 13. (left) Average of the 3-D isotropic Vs model, the best fit to the equation Vs = $V_0[(D + 1)^\alpha +1]$ is shown by the red dotted line. (right) Average of the 3-D radial anisotropy model.

a negative radial anisotropy. The lack of long period Love wave measurements prevents us to resolve the radial anisotropy at depths deeper than 3 km below mean sea level.

5.2. Maps and Cross Sections of the 3-D Voigt-Averaged Vs Model

The Vs isotropic model at each location is built following equation (2) by averaging the $n = 1000$ best Vsv and Vsh models:

$$Vs = \frac{1}{n} \sum_{i=1}^{n} Vs_i = \frac{1}{n} \sum_{i=1}^{n} \sqrt{\frac{2Vsv_i^2 + Vsh_i^2}{3}},$$

(5)

and its uncertainty is taken as the standard deviation of the mean. Similarly, the radial anisotropy model ξ at each location is computed following equation (1) with

$$\xi = \frac{1}{n} \sum_{i=1}^{n} \xi_i = \frac{1}{n} \sum_{i=1}^{n} \frac{Vsh_i - Vsv_i}{Vs_i},$$

(6)

and its uncertainty is taken as the standard deviation of the mean.

Initial parameterization is defined in terms of depth relative to the solid surface, then all models are shifted according to the altitude of the considered point to show values at depths relative to the sea level. Finally, the models are reinterpolated on a 200 m × 200 m × 100 m grid. Figure 13 shows the average isotropic Vs model and the average radial anisotropy model. The Vs model follows a power law profile which is well fitted by Vs = $131.1[(D + 1)^{0.3718} +1]$, where Vs is the shear wave velocity in m/s and D the depth below the surface in m with $D > 50$ m. This average model is removed from the 3-D Vs model to obtain the 3-D Vs anomaly model presented and interpreted in the following. Due to the lack of long period measurements in our data, the deepest parts of the model are less constrained and the uncertainties larger so we restrain the analysis of the model down to 3000 m bsl. On average, the absolute velocity uncertainty is <5% (3-D Vs, Vs-anomaly, anisotropy, Vs-uncertainty, and anisotropy-uncertainty models are available as supporting information along with a MATLAB code to plot profiles at different latitudes, longitudes, and depths inside the models.).

Examples of slices at constant elevation through the isotropic Vs model are presented in Figure 14. At 500 m above sea level, the velocity structure of the volcano appears dual: the East part showing higher velocities than the West part. At the sea level, the pattern is similar with the addition of a high-velocity corridor in the East-West direction passing below the summit. This latter anomaly becomes prominent at deeper depth, below 1000 m bsl and seems to link with another high-velocity anomaly below the Plaine des Sables. At all depths, the surroundings of the Enclos Fouqué caldera appear as low-velocity anomalies. Figure 15a profile shows an E-W section through this high-velocity anomaly corridor. Figure 15b profile is a section oriented North-South, perpendicular to this anomaly, passing through the volcano summit. Overlaid is the seismicity from the seismic crisis preceding the 9 March 1998 eruption of PdF Volcano located by *Battaglia et al.* [2005]. The migration of the seismicity toward the surface before the eruption shed light on the deep plumbing system of the volcano, highlighting the path taken by the magma to reach the surface. There is a very good agreement between the hypocenters location and a high-velocity plug reaching the sea level. Above sea level, the seismicity is offset to the East and seems to follow the limit between the high- and low-velocity anomalies below the central cone.

Our results show two other high-velocity anomalies: the largest one is located below the Grandes Pentes and Grand Brûlé (Figure 15a) on the eastern part of the volcano. The lack of station coverage prevents to reach the full extent of this anomaly on the East. A second anomaly, larger but similar in shape as the one below the summit is located below the Plaine des Sables. Low-velocity anomalies are mostly concentrated
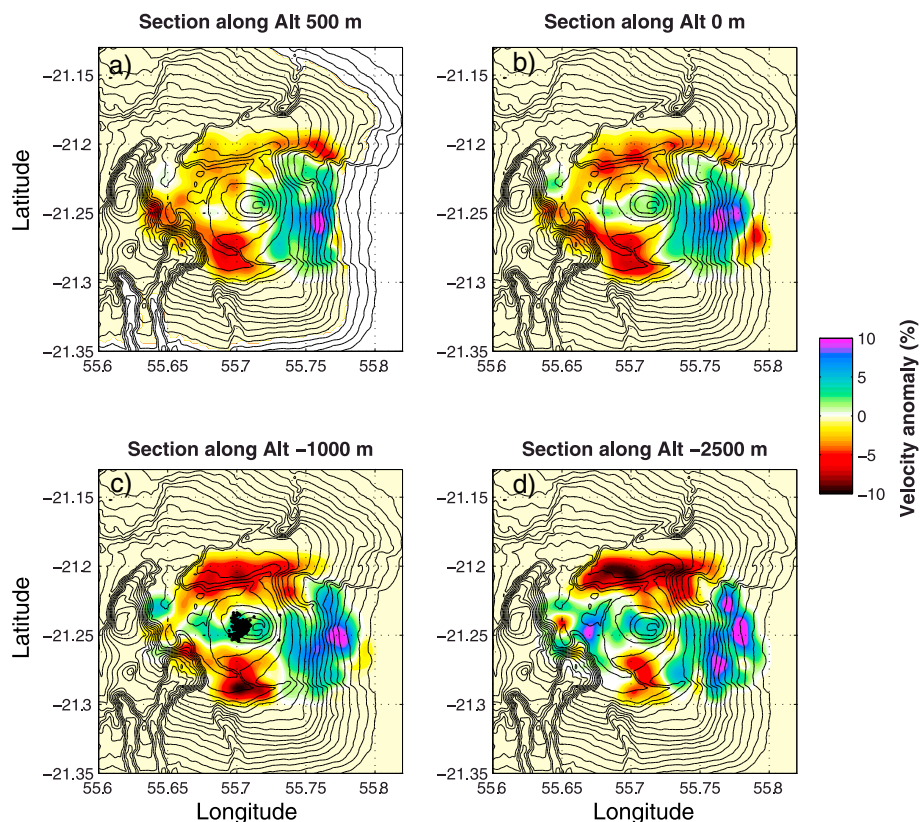
Figure 14. Slices through the isotropic Vs anomaly model at (a) 500 m above sea level, (b) 0 m, (c) −1000 m, and (d) −2500 m. Topography is shown by black contours. March 1998 intrusion seismicity is shown by black dots [*Battaglia et al.*, 2005] in the slice at −1000 m (only the hypocenters bsl).
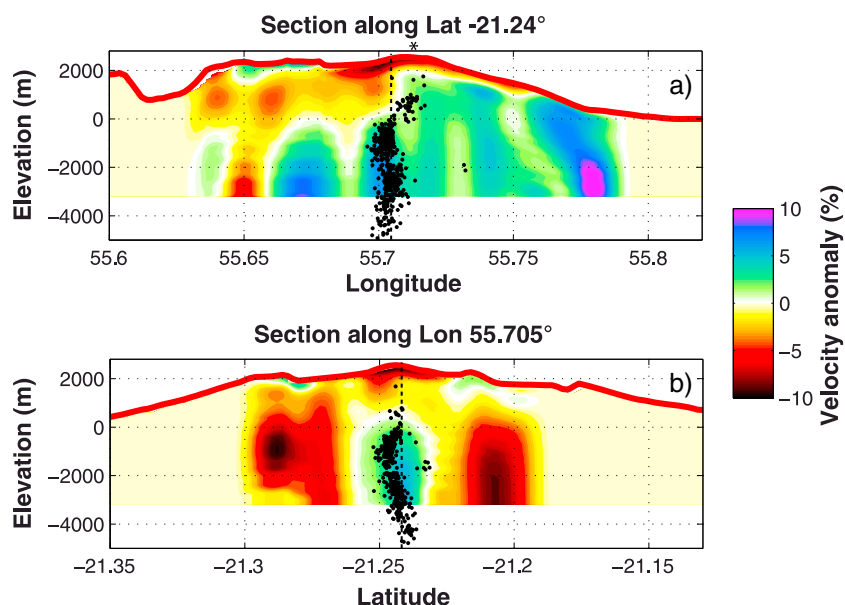

Figure 15. Vertical profiles through the isotropic Vs anomaly model. (a) EW profile at latitude −21.24°. (b) NS profile at longitude 55.705°. The thick red line is the local topography, and the black dots are the hypocenters from the 1998 intrusion [*Battaglia et al.*, 2005]. The thick dashed black lines show the intersection with the other profile. Asterisk on the top frame shows the location of the summit crater.
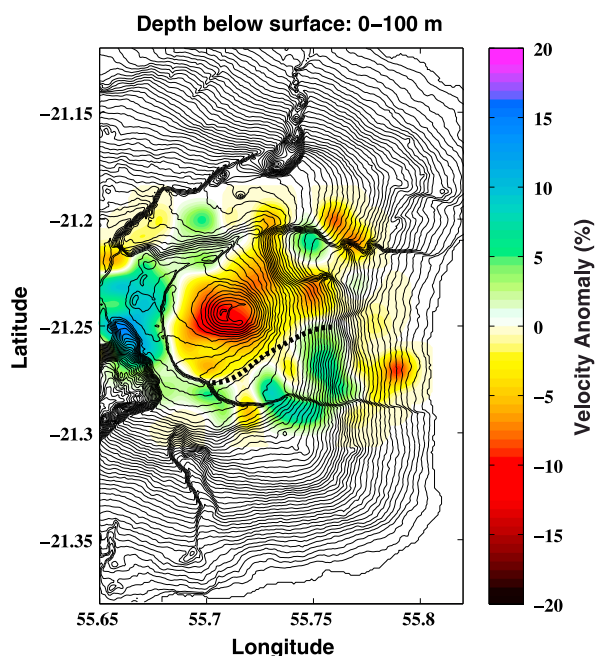
Figure 16. Isotropic shear wave velocity anomalies between 0 m and 100 m below the surface, following the topography. The dotted black line shows the approximate location of a topographical lineament discovered by *Michon and Saint-Ange* [2008] and interpreted as the result of a fault activity. The mean velocity is 645 m/s.

on the outer rim of the Enclos caldera, extending from the surface to 3 km bsl. The central cone is characterized by a very low velocity anomaly which seems to extend westward and at depth into a low-velocity layer between the surface and sea level (Figure 15a). Velocity anomalies of the very near surface down to 100 m below the surface are shown in Figure 16. The central cone and most of the ground of the Enclos Fouqué are characterized by low velocities at the exception of a southeastern part of the Enclos which exhibits higher velocities. These two regions are sharply separated by a linear topographical structure (∼100 m high) interpreted as the result of a normal fault activity in this area [*Michon and Saint-Ange*, 2008]. On the western part of the model, the Plaine des Sables area is characterized by a large high-velocity anomaly at the location of thick and dense lava flows [*Lénat et al.*, 2012]. The high resolution achieved in the near surface is due to the large number of short period measurements.
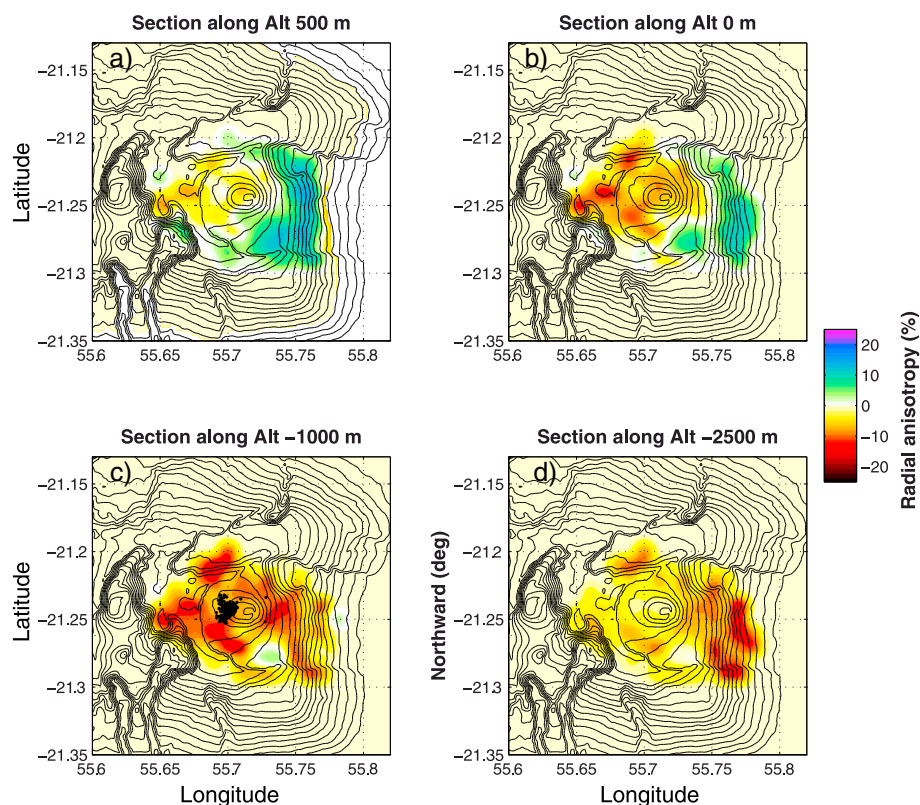

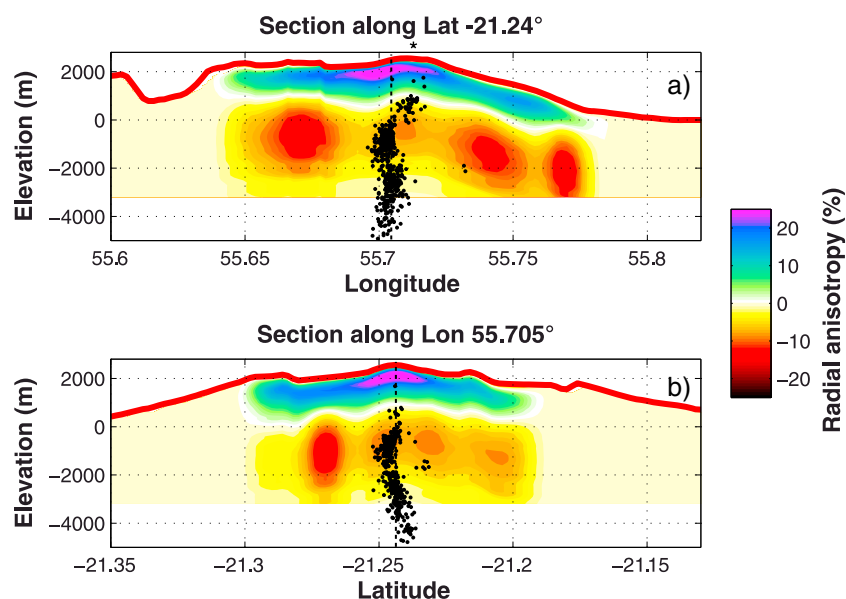**Figure 17.** Same as Figure 14 but for the radial anisotropy.

Figure 18. Same as Figure 15 but for the radial anisotropy.

5.3. Radial Anisotropy

The average radial anisotropy (Figure 13) presents three main features: a shallow negative anisotropy (Vsv > Vsh) above 100 m depth from the surface, then a strong positive anisotropy (Vsh > Vsv) between 100 m and 1500 m depth and finally another section of negative anisotropy below 1500 m. The fading of the anisotropy below 4000 m depth is mostly due to the lack of long period measurement in Love wave data. Nevertheless, the anisotropy results above 3000 bsl are quite well constrained. Even if the absolute values may have up to 50% of uncertainties in the deeper parts (see the anisotropy-uncertainty model in the supporting information), the sign of the anisotropy is very well constrained everywhere with more than 95% of the 1000 models showing this oscillatory pattern. Moreover, this specific pattern at depth is common throughout most of the studied area as shown by the maps at constant altitude (Figure 17) and the depth profiles (Figures 18a and 18b). The lateral variations of anisotropy are relatively small.

6. Discussion

The density of the seismic network and the availability of long period data allow to build for the first time a high-resolution shear wave velocity model of PdF Volcano down to 3 km bsl. The 3-D Vs model presented in this paper covers a large part of the Enclos Fouqué caldera where most of PdF volcanic activity occurs for about 4.5 ka [*Staudacher and Allègre*, 1993] as well as the Plaine des Sables. We can relate the structures seen in the model with structures observed in other studies by other geophysical and geological methods. *Lénat et al.* [2012] did a complete review on the different geophysical methods used on PdF and gathered their results to build a comprehensive model of the volcano. We based most of our interpretations on this model and the comparison between their Figures 5 and 6 and Figures 15a and 18a of the present paper.

The three deep high velocity anomalies are related with past and present preferential magma path intrusions. The most eastern anomaly, below the Grand Brûlé area is also the one exhibiting the largest positive amplitude. It is most certainly the imprint of Les Alizés Volcano magma chamber discovered by drilling [*Rançon et al.*, 1989] and imaged with gravimetry [*Rousset et al.*, 1989; *Malengreau et al.*, 1999; *Gailler et al.*, 2009]. The extent and shape of this structure are poorly known because of the difficulties to access the Grand Brûlé and the Grandes Pentes areas to perform geophysical investigations. Our model shows that the actual western extent of this dense core may be larger than previously estimated, as it could reach Grandes Pentes. The spatial resolution in this region, although not as good as around the central cone is still sufficient to retrieve an anomaly of the size of the width of Enclos Fouqué. However, the smearing is relatively strong in the East-West direction may prevent an accurate determination of its western extent.

The central deep high velocity anomaly below the summit has already been imaged with seismic tomography by *Nercessian et al.* [1996], *Hirn et al.* [1999], and *Brenguier et al.* [2007]. A later work by *Prôno et al.* [2009] does not seem to image this structure; however, the lateral extent and the lateral spatial resolution of their tomography may prevent to observe velocity contrasts with the neighboring regions. This high-velocity plug is neither detected by gravimetry, possibly because of the presence of shallow low density layers which hide the gravity signal from deeper parts [*Gailler et al.*, 2009]. Nonetheless, the fit with the March 1998 seismic crisis [*Battaglia et al.*, 2005] and the very good spatial resolution in this area lead us to interpret this anomaly as the present-day preferential magma path made of numerous solidified dikes.

Above it, at sea level, one can observe a strong velocity gradient separating the shallow low velocity structure of the volcano from its deep high velocity structure. This limit is rather flat on the western side of the edifice, following the sea level, and tends to become shallower on its eastern side when passing below the summit. This velocity gradient already observed by *Prôno et al.* [2009] acts as a structural discontinuity which controlled the migration of the 1998 seismicity toward the surface. This discontinuity may be related to the early formation of the edifice when it started to emerge from the ocean with its first aerial lava flows [*Oehler et al.*, 2005]. It could also be the limit between the ancient and eroded edifice of Les Alizés Volcano and the new edifice of PdF Volcano. This interpretation is strengthened by the radial anisotropy results. The separation between the deep negative anisotropy and the shallower positive one at about sea level (Figure 18a) suggests that the deeper part of the edifice is dominated by vertical structures which could be swarms of dykes built in the vicinity of the Les Alizés Volcano old magma chamber, whereas the part above sea level is dominated by horizontal structures: the thin lava flows from the young edifice of PdF Volcano. We limit our interpretations to the sign of the radial anisotropy because the simplifications we made during the inversion, neglecting the topography and the *P* wave anisotropy, may have biased its absolute value. However, as shown by *Xie et al.* [2013], the pure *S* wave radial anisotropy approximation tends to underestimate the anisotropy absolute value: the sign of it should therefore be robust. Besides, the inverted anisotropy does not seem to be strongly correlated with the topography so we believe that the actual anisotropic structure has robust signs and is 1-D at the first order (Figure 13). Nevertheless, it has to be reminded that it cannot be ruled out that cross-talk effects in the CCs, i.e., leakage of Rayleigh wave energy in the TT components, may bias the anisotropy results, particularly at long period and for large distances [*Haney et al.*, 2012]. Seeing that the negative anisotropy below sea level is rather weak with large uncertainties, it may be possible that the observed anisotropy is mostly apparent.

The third and most western deep high velocity anomaly located below the Plaine des Sables has clearly been imaged with gravimetry data as a dense intrusive core [e.g., *Gailler et al.*, 2009] and appears in *Lankar-Bénichou* [1997] seismic tomography results. This structure corresponds to the intrusive complex of the ancient PdF before it migrates to its present location about 150 ka ago [*Letourneur et al.*, 2008; *Merle et al.*, 2010]. The spatial resolution at that depth is not good enough to be able to discriminate whether there was an intermediate volcanic center between La Plaine des Sables and the present summit as suggested by *Letourneur et al.* [2008].

Above sea level, the PdF edifice presents an asymmetric velocity structure with the western side being slower that the eastern side (Figures 14 and 15a). This low-velocity layer may correspond to a highly conductive layer observed by *Lénat et al.* [2000]. They propose that this conductive layer could be a remnant of a zone of hydrothermal alteration developed around the ancient volcanic center. Moreover, hydrological modeling by *Join et al.* [2005] shows that on the western side of PdF, the top of the water table closely follows the top of the low- velocity layer, and the velocity of the water flow is smaller than on the East side. We hypothesize that the western low-velocity anomaly could be related to a stronger alteration of the volcanic deposits on this side of the edifice. This alteration could be due to either the presence of an ancient zone of hydrothermal alteration or to a longer stagnation of infiltrated meteoric water or a combination of both effects. The globally high velocity of the eastern flank of PdF is not well understood and contrasts with the low-velocity ring delineated by *Lankar-Bénichou* [1997] and *Hirn et al.* [1999]. The lack of other geophysical measurements in the Grandes Pentes due to the difficulty of access prevents us from bringing a definitive interpretation.

7. Conclusion

By jointly inverting group velocity dispersion curves of Rayleigh and Love waves measured from cross correlation of seismic noise recorded on Piton de la Fournaise Volcano, we were able to build a high-resolution 3-D model of the edifice shear wave velocity structure. This Vs model incorporates the radial anisotropy from the discrepancy between the Rayleigh and Love wave velocities and covers an area broader than previous seismic tomography models. The main results show three distinct high-velocity zones deeply rooted which corresponds to the hypovolcanic complex of the dismantled Les Alizés Volcano and ancient and present Piton de la Fournaise volcanic centers. Above sea level, the volcano presents an asymmetric velocity structure with a western flank slower than eastern one, probably due to a difference in rocks alteration. The measurements of group velocities at high frequency allow the near-surface results to be very consistent with the surface geology. The accurate determination of these near-surface velocities may help to better locate the volcano seismicity or the rockfalls which often happen near the summit [*Hibert et al.*, 2014]. The unprecedented measurement of the radial anisotropy on a hot spot volcano allowed us to image the limit between the ancient and recent edifices of Piton de la Fournaise where old structures are dominated by vertical intrusive dykes, whereas recent structures are mostly composed of horizontal lava flows. For comparison, the positive anisotropy observed below the Toba caldera indicates the presence of sills [*Jaxybulatov et al.*, 2014]. This implies that the radial anisotropy can be a very good indicator of the dominant fabric within the magmatic system and, consequently, of the dominant type of intrusions. Then, this might be used to evaluate the capacity of a given volcanic system to build large reservoirs and accumulate large volumes of stored magma in the crust. In a hot spot volcano like Piton de la Fournaise, the magma is quickly arriving from the mantle and is not stored for a long time at intermediate depths. The opposite occurs in large subduction zone volcanoes. By assessing the type of anisotropy present in volcanoes, one might have an idea of the residence time of the magma in the edifice.

This study also highlights the usefulness of dense seismic networks made of broadband sensors on and around volcanoes. The combination of data from stations near and far from the volcano coupled with the recording of a broad range of frequencies permits to draw more and more accurate pictures of the edifice deep and shallow structure. These images lead to a better understanding of the past and present behavior of the volcano which is the key to mitigate the risks due to its frequent eruptions.

Appendix A: Parameterization of the 1-D Velocity Profile

The complete parameterization of our 1-D velocity model requires 11 parameters (Figure 10): 10 are used to describe the velocity values as a function of depth and an additional parameter, P_d, is used to control the discretization of the velocity profile into 21 layers with constant velocities. Our velocity model is built as a power law backbone velocity profile (two parameters, α and V_0) [*Wathelet et al.*, 2004; *Mordret et al.*, 2014] overlaid by velocity anomalies parameterized by four cubic B splines (four parameters, S_1, S_2, S_3, and S_4, which are the weights of each spline). A set of cubic spline basis functions is fully defined by a knot vector and most precisely by the relative spacing between the knots. If the knots are equally spaced, whatever their values, the splines will be equally spaced and homogeneously distributed along the depth. However, in order to have a higher resolution near the surface, we used nonequally spaced knots with spacing increasing with depth. To do so, we raised the velocity-spline knot vector to the power of four. We parameterized the radial anisotropy with three cubic B splines (three parameters, S_5, S_6, and S_7). We added the possibility to vary the spacing between the anisotropy spline knots by raising them at the power of p, p ranging between 2 and 4, allowing a stretching or a compression of the radial anisotropy structure with depth. Besides, the first four knots set to zero force the anisotropy to be nonzero at the surface (see *Mégnin and Romanowicz* [2000] for more detailed discussion about velocity model B spline parameterization with nonequally spaced knots). We end up with a total of 10 free parameters to describe the velocity and anisotropy profile. The algorithm used for computing surface wave dispersion curves [*Herrmann and Ammon*, 2004] requires describing the structure as a set of layers with constant elastic properties. Therefore, to take into account the decrease of resolution with depth, we introduce an eleventh parameter and used 21 layers with varying logarithmically increasing depths for the 19 first as

$$D_i = 10^{\log P_d + \frac{i}{n_l - 2}\left(\log\left(\frac{9500}{P_d}\right)\right)} - P_d \tag{A1}$$

where D_i is the depth of the top of the ith layer (with i varying from 0 to 18), n_l, the number of layers, and P_d is the eleventh inverted parameter, with a depth dimension, controlling the depth distribution of the layers. Following results from a seismic study by *Gallart et al.* [1999], we set the top of the twentieth layer at 9 km depth below the surface with a velocity of 4 km/s and the top of the last layer is fixed at 15 km with a velocity of 5 km/s (Figure 10).

References

Aki, K., and K. Kaminuma (1963), Phase velocity of love waves in Japan (Part 1): Love waves from the Aleutian shock of March 9, 1957, *Bull. Earthquake Res. Inst.*, *41*(1), 243–259.

Anderson, D. L. (1962), Love wave dispersion in heterogeneous anisotropic media, *Geophysics*, *27*(4), 445–454.

Aoki, Y., et al. (2009), P-wave velocity structure beneath Asama Volcano, Japan, inferred from active source seismic experiment, *J. Volcanol. Geotherm. Res.*, *187*(3), 272–277.

Barmin, M., M. Ritzwoller, and A. Levshin (2001), A fast and reliable method for surface wave tomography, *Pure Appl. Geophys.*, *158*(8), 1351–1375.

Battaglia, J., V. Ferrazzini, T. Staudacher, K. Aki, and J.-L. Cheminée (2005), Pre-eruptive migration of earthquakes at the Piton de la Fournaise Volcano (Réunion Island), *Geophys. J. Int.*, *161*(2), 549–558.

Becker, T. W., B. Kustowski, and G. Ekström (2008), Radial seismic anisotropy as a constraint for upper mantle rheology, *Earth Planet. Sci. Lett.*, *267*(1), 213–227.

Beghein, C., J. Trampert, and H. Van Heijst (2006), Radial anisotropy in seismic reference models of the mantle, *J. Geophys. Res.*, *111*, B02303, doi:10.1029/2005JB003728.

Benz, H., B. Chouet, P. Dawson, J. Lahr, R. Page, and J. Hole (1996), Three-dimensional P and S wave velocity structure of Redoubt Volcano, Alaska, *J. Geophys. Res.*, *101*(B4), 8111–8128.

Bonnefoy-Claudet, S., F. Cotton, and P.-Y. Bard (2006), The nature of noise wavefield and its applications for site effects studies: A literature review, *Earth Sci. Rev.*, *79*(3), 205–227.

Brenguier, F., N. M. Shapiro, M. Campillo, A. Nercessian, and V. Ferrazzini (2007), 3-D surface wave tomography of the Piton de la Fournaise Volcano using seismic noise correlations, *Geophys. Res. Lett.*, *34*, L02305, doi:10.1029/2006GL028586.

Brenguier, F., et al. (2012), First results from the UnderVolc high resolution seismic and GPS network deployed on Piton de la Fournaise Volcano, *Seismol. Res. Lett.*, *83*(1), 97–102.

Campillo, M., and A. Paul (2003), Long-range correlations in the diffuse seismic coda, *Science*, *299*(5606), 547–549.

Chen, Y., J. Badal, and Z. Zhang (2009), Radial anisotropy in the crust and upper mantle beneath the Qinghai-Tibet Plateau and surrounding regions, *J. Asian Earth Sci.*, *36*(4), 289–302.

Courtillot, V., J. Besse, D. Vandamme, R. Montigny, J.-J. Jaeger, and H. Cappetta (1986), Deccan flood basalts at the Cretaceous/Tertiary boundary?, *Earth Planet. Sci. Lett.*, *80*(3), 361–374.

Di Stefano, R., and C. Chiarabba (2002), Active source tomography at Mt. Vesuvius: Constraints for the magmatic system, *J. Geophys. Res.*, *107*(B11), 2278, doi:10.1029/2001JB000792.

Duret, F., N. Shapiro, Z. Cao, V. Levin, P. Molnar, and S. Roecker (2010), Surface wave dispersion across Tibet: Direct evidence for radial anisotropy in the crust, *Geophys. Res. Lett.*, *37*, L16306, doi:10.1029/2010GL043811.

Dziewonski, A. M., and D. L. Anderson (1981), Preliminary reference Earth model, *Phys. Earth Planet. Inter.*, *25*(4), 297–356.

Ekström, G., and A. M. Dziewonski (1998), The unique anisotropy of the Pacific upper mantle, *Nature*, *394*(6689), 168–172.

Fichtner, A., and J. Trampert (2011), Resolution analysis in full waveform inversion, *Geophys. J. Int.*, *187*(3), 1604–1624.

Gailler, L.-S., and J.-F. Lénat (2012), Internal architecture of La Réunion (Indian Ocean) inferred from geophysical data, *J. Volcanol. Geotherm. Res.*, *221*, 83–98.

Gailler, L.-S., J.-F. Lénat, M. Lambert, G. Levieux, N. Villeneuve, and J.-L. Froger (2009), Gravity structure of Piton de la Fournaise Volcano and inferred mass transfer during the 2007 crisis, *J. Volcanol. Geotherm. Res.*, *184*(1), 31–48.

Gallart, J., L. Driad, P. Charvis, M. Sapin, A. Hirn, J. Diaz, B. Voogd, and M. Sachpazi (1999), Perturbation to the lithosphere along the hotspot track of la réunion from an offshore-onshore seismic transect, *J. Geophys. Res.*, *104*(B2), 2895–2908.

García-Yeguas, A., I. Koulakov, J. M. Ibáñez, and A. Rietbrock (2012), High resolution 3D P wave velocity structure beneath Tenerife Island (Canary Islands, Spain) based on tomographic inversion of active-source data, *J. Geophys. Res.*, *117*, B09309, doi:10.1029/2011JB008970.

Gebrande, H. (1982), 3.1.2.3 velocity-density relations, in *Subvolume B, Landolt-Börnstein - Group V Geophysics*, vol. 1b, edited by G. Angenheister, pp. 17–20, chap. Physical Properties of Rocks, Springer, Berlin, doi:10.1007/10201909_4.

Gouédard, P., et al. (2008), Cross-correlation of random fields: Mathematical approach and applications, *Geophys. Prospect.*, *56*(3), 375–393.

Gualtieri, L., E. Stutzmann, Y. Capdeville, F. Ardhuin, M. Schimmel, A. Mangeney, and A. Morelli (2013), Modelling secondary microseismic noise by normal mode summation, *Geophys. J. Int.*, *193*(3), 1732–1745.

Gutenberg, B. (1958), Microseisms, *Adv. Geophys.*, *5*, 53–92.

Haney, M. M., T. D. Mikesell, K. van Wijk, and H. Nakahara (2012), Extension of the spatial autocorrelation (SPAC) method to mixed-component correlations of surface waves, *Geophys. J. Int.*, *191*(1), 189–206.

Hasselmann, K. (1963), A statistical analysis of the generation of microseisms, *Rev. Geophys.*, *1*(2), 177–210.

Herrmann, R., and C. Ammon (2004), *Surface Waves, Receiver Functions and Crustal Structure*, Computer Programs in Seismology, St. Louis Univ., Mo.

Hibert, C., et al. (2014), Automated identification, location, and volume estimation of rockfalls at Piton de la Fournaise Volcano, *J. Geophys. Res. Earth Surf.*, *119*, 1082–1105, doi:10.1002/2013JF002970.

Hirn, A., et al. (1999), Structure interne du Piton de la Fournaise et de l'Etna d'après la tomographie sismique, in *Rapport Quadriennal 1995-1998*, edited by J. P. Barriot, pp. 129–136, CNFGG, Paris.

Jaxybulatov, K., N. Shapiro, I. Koulakov, A. Mordret, M. Landès, and C. Sens-Schönfelder (2014), A large magmatic sill complex beneath the Toba caldera, *Science*, *346*(6209), 617–619.

Jay, J. A., M. E. Pritchard, M. E. West, D. Christensen, M. Haney, E. Minaya, M. Sunagua, S. R. McNutt, and M. Zabala (2012), Shallow seismicity, triggered seismicity, and ambient noise tomography at the long-dormant Uturuncu Volcano, Bolivia, *Bull. Volcanol.*, *74*(4), 817–837.

Join, J.-L., J.-L. Folio, and B. Robineau (2005), Aquifers and groundwater within active shield volcanoes. Evolution of conceptual models in the Piton de la Fournaise Volcano, *J. Volcanol. Geotherm. Res.*, *147*(1), 187–201.

Koulakov, I., E. I. Gordeev, N. L. Dobretsov, V. A. Vernikovsky, S. Senyukov, and A. Jakovlev (2011), Feeding volcanoes of the Kluchevskoy group from the results of local earthquake tomography, *Geophys. Res. Lett.*, *38*, L09305, doi:10.1029/2011GL046957.

Laigle, M., A. Hirn, M. Sapin, J.-C. Lépine, J. Diaz, J. Gallart, and R. Nicolich (2000), Mount Etna dense array local earthquake P and S tomography and implications for volcanic plumbing, *J. Geophys. Res.*, *105*(B9), 21,633–21,646.

Lankar-Bénichou, V. (1997), Approches par tomographie sismique du Piton de la Fournaise, La Réunion, PhD thesis, Institut de physique du globe, Paris.

Lees, J. M. (1992), The magma system of Mount St. Helens: Non-linear high-resolution P-wave tomography, *J. Volcanol. Geotherm. Res.*, *53*(1), 103–116.

Lénat, J.-F., D. Fitterman, D. B. Jackson, and P. Labazuy (2000), Geoelectrical structure of the central zone of Piton de la Fournaise Volcano (Réunion), *Bull. Volcanol.*, *62*(2), 75–89.

Lénat, J.-F., B. Gibert-Malengreau, and A. Galdéano (2001), A new model for the evolution of the volcanic island of Reunion (Indian Ocean), *J. Geophys. Res.*, *106*(B5), 8645–8663.

Lénat, J.-F., P. Bachèlery, and O. Merle (2012), Anatomy of Piton de la Fournaise Volcano (La Réunion, Indian Ocean), *Bull. Volcanol.*, *74*(9), 1945–1961.

Letourneur, L., A. Peltier, T. Staudacher, and A. Gudmundsson (2008), The effects of rock heterogeneities on dyke paths and asymmetric ground deformation: The example of Piton de la Fournaise (Réunion Island), *J. Volcanol. Geotherm. Res.*, *173*(3), 289–302.

Levshin, A., T. Yanovskaya, A. Lander, B. Bukchin, M. Barmin, L. Ratnikova, and E. Its (1989), *Seismic Surface Waves in a Laterally Inhomogeneous Earth*, Kluwer, Dordrecht.

Lin, F., M. Ritzwoller, J. Townend, S. Bannister, and M. Savage (2007), Ambient noise Rayleigh wave tomography of New Zealand, *Geophys. J. Int.*, *170*(2), 649–666.

Lin, F., M. Moschetti, and M. Ritzwoller (2008), Surface wave tomography of the western United States from ambient seismic noise: Rayleigh and Love wave phase velocity maps, *Geophys. J. Int.*, *173*(1), 281–298.

Lin, F.-C., M. H. Ritzwoller, Y. Yang, M. P. Moschetti, and M. J. Fouch (2011), Complex and variable crustal and uppermost mantle seismic anisotropy in the western United States, *Nat. Geosci.*, *4*(1), 55–61.

Lin, G., P. M. Shearer, R. S. Matoza, P. G. Okubo, and F. Amelung (2014), Three-dimensional seismic velocity structure of Mauna Loa and Kilauea Volcanoes in Hawaii from local seismic tomography, *J. Geophys. Res. Solid Earth*, *119*, 4377–4392, doi:10.1002/2013JB010820.

Longuet-Higgins, M. (1950), A theory of the origin of microseisms, *Philos. Trans. R. Soc. London, Ser. A*, *243*(857), 1–35.

Love, A. E. H. (1927), *A Treatise on the Mathematical Theory of Elasticity*, Cambridge Univ. Press, Cambridge, U. K.

Luzón, F., J. Almendros, and A. García-Jerez (2011), Shallow structure of Deception Island, Antarctica, from correlations of ambient seismic noise on a set of dense seismic arrays, *Geophys. J. Int.*, *185*(2), 737–748.

Malengreau, B., J.-F. Lénat, and J.-L. Froger (1999), Structure of Réunion Island (Indian Ocean) inferred from the interpretation of gravity anomalies, *J. Volcanol. Geotherm. Res.*, *88*(3), 131–146.

Masterlark, T., M. Haney, H. Dickinson, T. Fournier, and C. Searcy (2010), Rheologic and structural controls on the deformation of Okmok Volcano, Alaska: FEMs, InSAR, and ambient noise tomography, *J. Geophys. Res.*, *115*, B02409, doi:10.1029/2009JB006324.

Mégnin, C., and B. Romanowicz (2000), The three-dimensional shear velocity structure of the mantle from the inversion of body, surface and higher-mode waveforms, *Geophys. J. Int.*, *143*(3), 709–728.

Merle, O., P. Mairine, L. Michon, P. Bachèlery, and M. Smietana (2010), Calderas, landslides and paleo-canyons on Piton de la Fournaise Volcano (La Réunion Island, Indian Ocean), *J. Volcanol. Geotherm. Res.*, *189*(1), 131–142.

Michon, L., and F. Saint-Ange (2008), Morphology of Piton de la Fournaise basaltic shield volcano (La Réunion Island): Characterization and implication in the volcano evolution, *J. Geophys. Res.*, *113*, B03203, doi:10.1029/2005JB004118.

Michon, L., F. Saint-Ange, P. Bachelery, N. Villeneuve, and T. Staudacher (2007), Role of the structural inheritance of the oceanic lithosphere in the magmato-tectonic evolution of Piton de la Fournaise Volcano (La Réunion Island), *J. Geophys. Res.*, *112*, B04205, doi:10.1029/2006JB004598.

Montagner, J.-P., and T. Tanimoto (1991), Global upper mantle tomography of seismic velocities and anisotropies, *J. Geophys. Res.*, *96*(B12), 20,337–20,351.

Mordret, A., M. Landès, N. Shapiro, S. Singh, P. Roux, and O. Barkved (2013), Near-surface study at the Valhall oil field from ambient noise surface wave tomography, *Geophys. J. Int.*, *193*(3), 1627–1643.

Mordret, A., M. Landès, N. Shapiro, S. Singh, and P. Roux (2014), Ambient noise surface wave tomography to determine the shallow shear velocity structure at Valhall: Depth inversion with a Neighbourhood Algorithm, *Geophys. J. Int.*, *198*(3), 1514–1525.

Moschetti, M., M. Ritzwoller, and N. Shapiro (2007), Surface wave tomography of the western United States from ambient seismic noise: Rayleigh wave group velocity maps, *Geochem. Geophys. Geosyst.*, *8*, Q08010, doi:10.1029/2007GC001655.

Moschetti, M., M. Ritzwoller, F. Lin, and Y. Yang (2010), Seismic evidence for widespread western-US deep-crustal deformation caused by extension, *Nature*, *464*(7290), 885–889.

Nagaoka, Y., K. Nishida, Y. Aoki, M. Takeo, and T. Ohminato (2012), Seismic imaging of magma chamber beneath an active volcano, *Earth Planet. Sci. Lett.*, *333*, 1–8.

Nercessian, A., A. Hirn, J.-C. Lépine, and M. Sapin (1996), Internal structure of Piton de la Fournaise Volcano from seismic wave propagation and earthquake distribution, *J. Volcanol. Geotherm. Res.*, *70*(3), 123–143.

Oehler, J.-F., B. van Wyk de Vries, and P. Labazuy (2005), Landslides and spreading of oceanic hot-spot and arc shield volcanoes on Low Strength Layers (LSLs): An analogue modeling approach, *J. Volcanol. Geotherm. Res.*, *144*(1), 169–189.

Prôno, E., J. Battaglia, V. Monteiller, J.-L. Got, and V. Ferrazzini (2009), P-wave velocity structure of Piton de la Fournaise Volcano deduced from seismic data recorded between 1996 and 1999, *J. Volcanol. Geotherm. Res.*, *184*(1), 49–62.

Rançon, J. P., P. Lerebour, and T. Augé (1989), The Grand Brûlé exploration drilling: New data on the deep framework of the Piton de la Fournaise Volcano. Part 1: Lithostratigraphic units and volcanostructural implications, *J. Volcanol. Geotherm. Res.*, *36*(1), 113–127.

Ritzwoller, M. H., F.-C. Lin, and W. Shen (2011), Ambient noise tomography with a large seismic array, *C. R. Geosci.*, *343*(8), 558–570.

Rousset, D., A. Lesquer, A. Bonneville, and J. F. Lénat (1989), Complete gravity study of Piton de la Fournaise Volcano, Réunion Island, *J. Volcanol. Geotherm. Res.*, *36*(1), 37–52.

Sabra, K., P. Gerstoft, P. Roux, W. Kuperman, and M. Fehler (2005), Surface wave tomography from microseisms in Southern California, *Geophys. Res. Lett.*, *32*, L14311, doi:10.1029/2005GL023155.

Sambridge, M. (1999), Geophysical inversion with a Neighbourhood Algorithm—I. Searching a parameter space, *Geophys. J. Int.*, *138*(2), 479–494.

Shalev, E., et al. (2010), Three-dimensional seismic velocity tomography of Montserrat from the SEA-CALIPSO offshore/onshore experiment, *Geophys. Res. Lett.*, 37, L00E17, doi:10.1029/2010GL042498.

Shapiro, N., M. Campillo, L. Margerin, S. Singh, V. Kostoglodov, and J. Pacheco (2000), The energy partitioning and the diffusive character of the seismic coda, *Bull. Seismol. Soc. Am.*, 90(3), 655–665.

Shapiro, N. M., and M. Campillo (2004), Emergence of broadband Rayleigh waves from correlations of the ambient seismic noise, *Geophys. Res. Lett.*, 31, L07614, doi:10.1029/2004GL019491.

Shapiro, N. M., and M. Ritzwoller (2002), Monte-Carlo inversion for a global shear-velocity model of the crust and upper mantle, *Geophys. J. Int.*, 151(1), 88–105.

Shapiro, N. M., M. H. Ritzwoller, P. Molnar, and V. Levin (2004), Thinning and flow of Tibetan crust constrained by seismic anisotropy, *Science*, 305(5681), 233–236.

Shapiro, N. M., M. Campillo, L. Stehly, and M. Ritzwoller (2005), High-resolution surface-wave tomography from ambient seismic noise, *Science*, 307(5715), 1615–1618.

Stankiewicz, J., T. Ryberg, C. Haberland, Fauzi, and D. Natawidjaja (2010), Lake Toba Volcano magma chamber imaged by ambient seismic noise tomography, *Geophys. Res. Lett.*, 37, L17306, doi:10.1029/2010GL044211.

Staudacher, T., and C. J. Allègre (1993), Ages of the second caldera of Piton de la Fournaise Volcano (Réunion) determined by cosmic ray produced 3He and 21Ne, *Earth Planet. Sci. Lett.*, 119(3), 395–404.

Stehly, L., B. Fry, M. Campillo, N. M. Shapiro, J. Guilbert, L. Boschi, and D. Giardini (2009), Tomography of the Alpine region from observations of seismic ambient noise, *Geophys. J. Int.*, 178(1), 338–350.

Tanaka, S., et al. (2002), Three-dimensional *P*-wave velocity structure of Iwate Volcano, Japan from active seismic survey, *Geophys. Res. Lett.*, 29(10), 59-1–59-4, doi:10.1029/2002GL014983.

Villagómez, D. R., D. R. Toomey, E. E. Hooft, and S. C. Solomon (2011), Crustal structure beneath the Galápagos Archipelago from ambient noise tomography and its implications for plume-lithosphere interactions, *J. Geophys. Res.*, 116, B04310, doi:10.1029/2010JB007764.

Waite, G. P., and S. C. Moran (2009), Vp structure of Mount St. Helens, Washington, USA, imaged with local earthquake tomography, *J. Volcanol. Geotherm. Res.*, 182(1), 113–122.

Wapenaar, K. (2004), Retrieving the elastodynamic Green's function of an arbitrary inhomogeneous medium by cross correlation, *Phys. Rev. Lett.*, 93(25), 254301.

Wathelet, M., D. Jongmans, and M. Ohrnberger (2004), Surface wave inversion using a direct search algorithm and its application to ambient vibration measurements, *Near Surf. Geophys.*, 2(4), 211–221.

Weaver, R., and O. Lobkis (2001), Ultrasonics without a source: Thermal fluctuation correlations at MHz frequencies, *Phys. Rev. Lett.*, 87(13), 134301.

Xie, J., M. H. Ritzwoller, W. Shen, Y. Yang, Y. Zheng, and L. Zhou (2013), Crustal radial anisotropy across eastern Tibet and the western Yangtze craton, *J. Geophys. Res. Solid Earth*, 118, 4226–4252, doi:10.1002/jgrb.50296.

Yang, Y., M. Ritzwoller, A. Levshin, and N. M. Shapiro (2007), Ambient noise Rayleigh wave tomography across Europe, *Geophys. J. Int.*, 168, 259–274.

Zandomeneghi, D., R. Aster, P. Kyle, A. Barclay, J. Chaput, and H. Knox (2013), Internal structure of Erebus Volcano, Antarctica imaged by high-resolution active-source seismic tomography and coda interferometry, *J. Geophys. Res. Solid Earth*, 118, 1067–1078, doi:10.1002/jgrb.50073.

Zheng, S., X. Sun, X. Song, Y. Yang, and M. Ritzwoller (2008), Surface wave tomography of China from ambient seismic noise correlation, *Geochem. Geophys. Geosyst.*, 9, Q05020, doi:10.1029/2008GC001981.

Zheng, Y., W. Shen, L. Zhou, Y. Yang, Z. Xie, and M. H. Ritzwoller (2011), Crust and uppermost mantle beneath the North China Craton, northeastern China, and the Sea of Japan from ambient noise tomography, *J. Geophys. Res.*, 116, B12312, doi:10.1029/2011JB008637.